

Model testing of a floating wave energy converter with an internal U-shaped oscillating water column

S. Ribeiro e Silva^a, R.P.F. Gomes^{b,*}, B.S. Lopes^b, A.A.D. Carrelhas^b, L.M.C. Gato^b, J.C. C. Henriques^b, J.M. Gordo^a, A.F.O. Falcão^b

^a CENTEC, Instituto Superior Técnico, Universidade de Lisboa, Av. Rovisco Pais 1, 1049-001 Lisboa, Portugal

^b IDMEC, Instituto Superior Técnico, Universidade de Lisboa, Av. Rovisco Pais 1, 1049-001 Lisboa, Portugal

ARTICLE INFO

Keywords:

Wave energy
Oscillating water column
U-shaped tank
Wave tank testing

ABSTRACT

The development of wave energy converters is centred on the combination of two factors: cost-effectiveness of energy extraction and system survivability on extreme sea conditions. Despite advances in numerical modelling, wave tank model testing still presents the most reliable option to evaluate these two factors. This paper presents an experimental study on the hydrodynamic responses of the UGEN, a wave energy converter consisting of an asymmetric floater with an internal U-shaped tank partially filled with water. The device absorbs energy through the oscillating-water-column (OWC) motion inside the U-shaped tank, induced by the wave action on the floater. The experimental testing of a bottom-moored 1:24th-scale model was performed at the COAST Laboratory, University of Plymouth, UK, considering regular and irregular wave conditions. The wave tank test measurements report six-degree-of-freedom rigid-body motions, mean drift forces, OWC motion, structural stresses and mooring loads. Results present the characterization of the energy absorption at the internal OWC induced by the floater's sway, heave and roll. The occurrence of low-cycle auto-parametric resonance under certain wave conditions was detected and induced large roll motions, which affected power extraction and increased mooring line loads, particularly for large wave amplitudes.

1. Introduction

Over the last decades, several alternatives to electrical generation from fossil fuel sources have been investigated. Wave energy has shown to be one of the most promising options, displaying an energetic potential comparable with the actual world electricity consumption [1]. The main technological challenge has been developing a robust device that can efficiently extract energy compared to other renewable energy sources and survive extreme sea conditions.

A wide variety of wave energy converters (WECs) have been developed and tested over the last fifty years [2]. UGEN is a WEC based on the oscillating water column (OWC) principle patented by Instituto Superior Técnico (IST) in 2010 [3]. The device is composed of two components: (i) the asymmetric floater and (ii) a power take-off (PTO) system composed of a self-rectifying air turbine directly coupled to an electrical generator [4,5]. All moving parts of the WEC are encapsulated inside the hull for robustness. The UGEN extracts energy through the relative

rotational motion as in the case of the Edinburgh Duck (also known as Salter's "duck") [6], SEAREV [7], PeWEC [8], WITT [9] and E-motions [10].

Under a wide range of incident wave conditions, the asymmetric floater is excited in three modes: roll, sway and heave. This excitation results in the relative motion of the OWC inside the inner U-tank that compresses and expands the air of two opposite chambers. The pressure difference between the two air chambers generates an airflow through a self-rectifying turbine that drives the electrical generator (see Fig. 1a,c, d).

The UGEN combines an oscillating body with an internal OWC system, as the OWC is not directly excited by the waves. The concept was inspired by the U-shaped tanks used for ship roll stabilization [11,12]. For ships, the roll motion has many adverse effects on operations and comfort onboard and therefore should be minimized. In the case of UGEN WEC, this motion corresponds to the major driver and, therefore, is highly desirable, so both the floater and the U-tank dimensions and

* Corresponding author.

E-mail addresses: ribeiro.e.silva@tecnico.ulisboa.pt (S. Ribeiro e Silva), ruigomes@tecnico.ulisboa.pt (R.P.F. Gomes), barbara.lopes@tecnico.ulisboa.pt (B.S. Lopes), ana.carrelhas@tecnico.ulisboa.pt (A.A.D. Carrelhas), luis.gato@tecnico.ulisboa.pt (L.M.C. Gato), joaochenriques@tecnico.ulisboa.pt (J.C.C. Henriques), jose.gordo@tecnico.ulisboa.pt (J.M. Gordo), antonio.falcao@tecnico.ulisboa.pt (A.F.O. Falcão).

<https://doi.org/10.1016/j.enconman.2021.114211>

Received 18 December 2020; Accepted 21 April 2021

Available online 12 May 2021

0196-8904/© 2021 Elsevier Ltd. All rights reserved.

geometries should be designed to promote roll motion and maximize power extraction efficiency.

A similar device, also depending on the pitch motion (herein designated as roll motion) for power extraction, is the BBDB (Backward Bent Duct Buoy). This WEC is a floating structure containing an inner L-shaped OWC open backwards to the wave action [13,14]. Incident waves induce roll motion in the UGEN as in the case of Refs. [6–10,13].

Asymmetric floater geometries result in more efficient WECs as indicated by the linear theory of oscillating bodies [15] and supported by optimization studies [16,7]. Another advantage of oscillating bodies lies in the ability to control the power take-off to tune the system to resonance [17]. Studies have shown promising capture width ratios: 0.47 for the Edinburgh Duck; 0.25 for the SEAREV; and 0.35 for the BBDB [18].

The exponential decay of the wave energy with the depth makes the devices' submergence a highly desired feature during storm conditions. A fundamental characteristic of the UGEN device is the simplicity of submergence in extreme wave conditions. The submergence operations only require the flooding of the ballast compartments with seawater using remotely operated bottom valves. To restore floatability, a compressed-air reservoir installed inside the device injects air in the ballast compartments via a remotely operated air valve to expel the seawater throughout the same bottom valves.

The UGEN was designed to be intrinsically robust and reliable due to:

- absence of moving parts in contact with seawater;
- the OWC is enclosed totally inside the hull;
- the device ability to become excited under “standard” resonant conditions (excitation wave period equal to natural roll period);
- the occurrence of low-cycle auto-parametric resonance (excitation wave period equal to half the natural roll period), which can increase the capture width ratio for less energetic sea states;
- the device submergence under extreme sea conditions reduces the wave-induced structural loads.

The designers can take advantage of the hull water tightness to further reduce the Levelized Cost of Energy (LCoE) considering that:

- the hull interior can be pressurized above the local absolute hydrostatic pressure under submergence conditions to reduce structural compressive mechanical stresses;
- decreasing compressive mechanical stresses reduces the hull structural cost and the project's total CAPEX;
- the air chamber pressure can be increased to rise the turbine power output by increasing the air density (non-linear effect).

The UGEN wave energy converter concept has been under development since 2010 and already completed several developing stages. Tests at 1:16th-scale were carried out in 2010 at IFREMER (Brest, France) ocean basin, within the framework of the 1st call of the FP7-METRI programme [19,20]. These experiments validated the concept under operational sea conditions and assessed the UGEN's performance. A numerical model based on potential flow theory was developed to estimate the annual-averaged power output of the device [21,22]. Later, the hull geometry and the PTO characteristics were optimized, to maximize the annual-averaged absorbed power at a location in the North Atlantic Ocean [23]. The optimization results show substantial capture width ratio improvements when compared with previous designs.

Different types of self-rectifying turbines can be installed in UGEN's PTO system [4,5]. One favoured option due to its simplicity and easy integration with UGEN's internal OWC configuration is the well-known Wells turbine [24]. Another possibility is the biradial turbine designed to overcome the Wells turbine's efficiency limitations, specifically the efficiency drop above a critical flow rate [25]. This novel turbine was demonstrated in sea trials at Mutriku breakwater wave power plant and at the IDOM MARMOK A5 spar-buoy deployed at BIMEP test site [26,27].

The current research status still presents some shortcomings covered in this work. Numerical models of the UGEN disregard detailed viscous flow effects and mooring line forces [19,20]. The current study addresses these issues and examines the new optimized UGEN hull's performance under operational and extreme wave conditions.

The experimental tests were carried out at the COAST Laboratory of the University of Plymouth (UoP), UK, under the MaRINET2 Infrastructures Network (Horizon 2020) EU project. A bottom moored

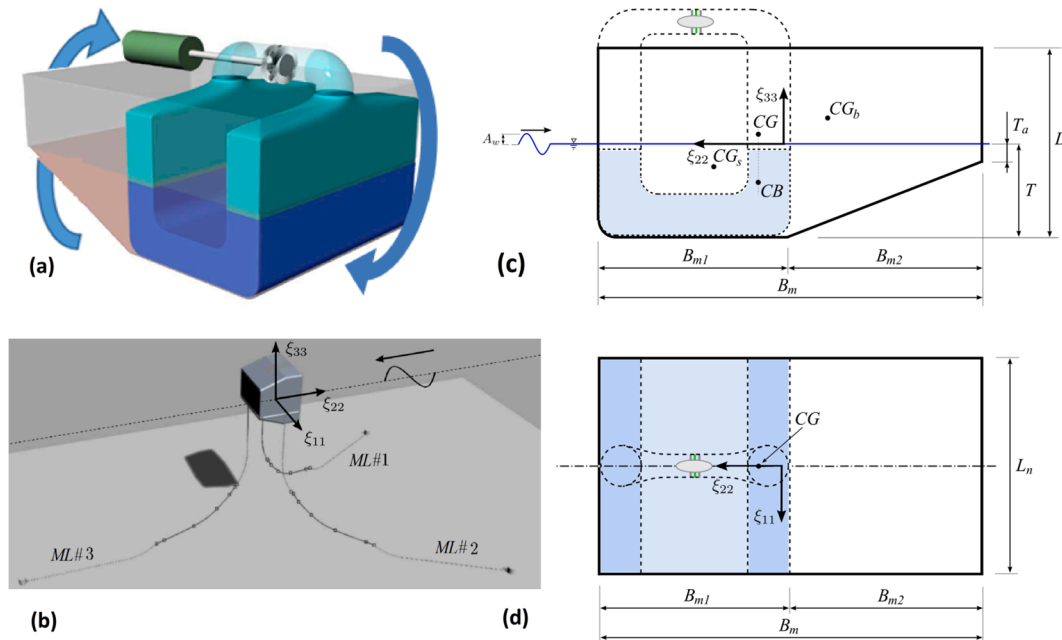


Fig. 1. (a) The UGEN asymmetric floater is equipped with a U-tank partially filled with water to create an internal OWC. A self-rectifying air turbine connects the two lateral air chambers and drives the electrical generator. (b) The mooring system comprises three lines composed of three segments from anchor to fairlead. (c) Lateral cut-section view and (d) top view of the UGEN device showing the U-tank.

1:24th-scale model of the UGEN device was built for the wave tank tests. The turbine was simulated using a perforated disk to impose a quadratic relationship between the turbine's pressure drop and mass flow rate. The experimental measurements allowed investigation of the rigid-body motions, mean drift effects, OWC motions, structural stresses and mooring loads. These experimental tests assessed real fluid effects and non-linear hydrodynamic effects induced by extreme sea conditions in the device operation.

The measurement of wave-induced structural and mooring loads will be utilized to validate numerical models and decide whether temporary submergence under extreme wave conditions has advantages over the always-floating configuration. Additionally, the experimental work verifies the possibility of extracting power under low-cycle auto-parametric resonance conditions in both regular and irregular waves (see [28–30]). These parameters' knowledge is the key to an accurate assessment of the LCoE.

The remaining of the paper is organized as follows. Section 2 presents the description and principle of operation of the UGEN device. The experimental apparatus and the model are described in Section 3. Experimental results and their detailed analysis appear in Section 4. Finally, Section 5 presents the conclusions and future work.

2. The UGEN device

In most common OWC devices [31], the turbine is installed in a duct that connects the air chamber to the atmosphere. The UGEN device uses an alternative arrangement where two independent enclosed air chambers are connected through a duct where the turbine is installed. This closed system configuration allows active control of the U-tank water level to increase the capture width and reduce the LCoE. In practice, this active control can be implemented via bidirectional freshwater transfer between a reservoir located inside the U-tank and the OWC.

In this work and all previous studies addressing the UGEN technology, the adopted coordinate system has been the same as the one traditionally used in U-tank ship roll stabilization, see Fig. 2. Waves travelling in ξ_{22} direction excite the device mainly in roll ξ_{44} but heave ξ_{33} and sway ξ_{22} motions also contribute to the wave energy absorption due to the hull asymmetric form. Roll combined with heave and sway motions of the floater induces the oscillation of the internal OWC ξ_{77} . The device dynamics are characterized by the roll natural damped frequency of the hull and the OWC angular oscillations. Previous studies [21] concluded that the system performs better if the two natural frequencies are separated and by having the OWC natural frequency higher than the natural roll frequency.

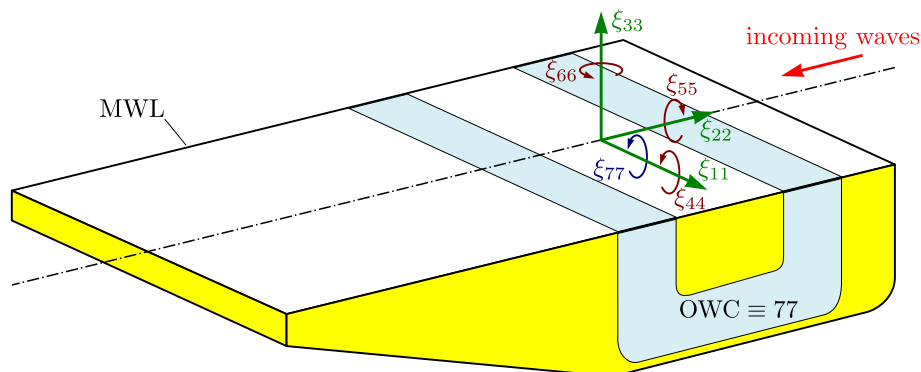


Fig. 2. The adopted coordinate system where the six-degree of freedom are denoted as: surge ξ_{11} , sway ξ_{22} , heave ξ_{33} , roll ξ_{44} , pitch ξ_{55} and yaw ξ_{66} . Note that the incident waves are along the ξ_{22} axis.

3. Experimental set-up

3.1. Experimental apparatus

The experimental tests were performed in the UoP COAST Ocean Basin, Fig. 3. This basin is a wave generation facility with 24 flap-type paddles capable of producing regular and irregular waves for different water depths. The basin is 35 m-long, 15.5 m-wide, and its moveable floor allows a maximum water depth of 3 m.

The UGEN model is illustrated in Figs. 3–5. The model and its mooring system were designed, constructed, equipped and instrumented in Portugal before being tested in Plymouth.

The model was manufactured using welded mild steel plates and profiles and was equipped with one removable hatch cover on top and two more removable hatch covers at the bottom to gain access to the ballast/de-ballast compartments. The ballast/de-ballast circuit was installed inside those compartments during the manufacture of the model and included among other items a PVC piping circuit for water, a rubber piping circuit for compressed air, a 0.015 m³ bottle for compressed air at 200 bar fitted with a pressure reducer, and remotely operated air- and water-valves to allow the submergence and emergence of the model in extreme sea states. Preliminary submergence tests were performed at the Portuguese Navy Diving Centre to confirm the floating structure's water tightness.

Four conductive wave gauges were positioned in the basin to measure free-surface elevations caused by wave propagation. The wave gauge data was acquired at 128 Hz after daily calibration. The calibration error presented was smaller than 0.95 mm.

The incident wave characteristics were determined by a wave gauge positioned aside the model. This wave gauge's free-surface elevation values were compared with the measurements obtained without the model showing negligible differences, and therefore, a small influence from the model's radiated and scattered waves. These tests also demonstrated that the wavemaker reproduced the imposed sea states and the repeatability of the time series.

A Qualisys motion tracking system consisting of six infrared cameras and reflective targets on the top of the model was used to acquire the model's six-degree-of-freedom time series. The motion data was acquired at a rate of 100 Hz with a typical measurement error of 0.5 mm. However, the error reached 4 mm under extreme wave conditions.

The pressure difference between the two UGEN air chambers was measured with a differential pressure transducer (± 2.5 kPa) to allow the computation of the instantaneous pneumatic power available to the turbine.

Two echo-sounder sensors were installed at the top of each air chamber to measure the instantaneous OWC free-surface position, enabling the determination of the instantaneous inclination angle of the water inside the U-tank.



Fig. 3. (a) General view of the ocean wave basin facility; (b) 3D CAD view of the 1:24th-scaled model of the UGEN WEC; and (c) View of the 1:24th-scaled model of the UGEN WEC and the wave gauges during tests at UoP COAST Ocean Basin, Plymouth, UK.

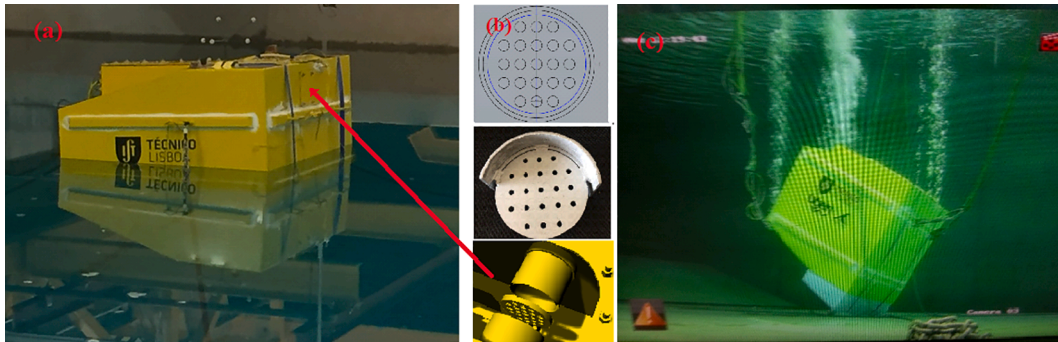


Fig. 4. (a) View of the floating UGEN model in the wave tank. (b) Snapshots of the PTO simulator (perforated disk of 90 mm diameter with 21 circular orifices) and schematic representation of its application in the model. (c) View of the UGEN model in the submerged scenario during experimental tests.

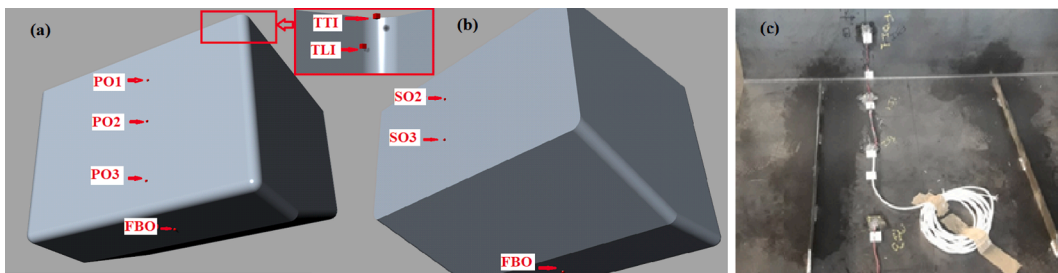


Fig. 5. (a) The three strain gauges installed in the hull's port board outer side (PO) and the flat bottom (FB) strain gauge. The detail box shows the strain gauges located at the U-tank top inner side (TTI) and U-tank lateral inner side (TLI). (b) Starboard side (S) strain gauges. (c) Picture of four strain gauges FBI, PII, PI2 and PI3, with the corresponding signal cables connecting to the data acquisition system.

An LSB-210 Futek analogue submersible S-Beam Junior load cell was installed at each fairlead to monitor the mooring lines tension. The load cell had a range of ± 445 N and a non-linearity of 0.2% of the rated output value.

All the signals except the wave gauges and the Qualysis Motion Tracking systems were acquired at 1667 Hz by a National Instruments DAQ hardware paired with custom written LabView software.

The procedure suggested by [32] was adopted to estimate the uncertainty of the measurements. The manufacturers provided the random error for the echo-sounders, the differential pressure sensors, and the mooring load cells. These were combined with the estimates of the bias errors to predict the overall confidence limits. Percentage uncertainties in pressure difference readings are of the order of 4% for the moderate sea states and 2% for the rough sea states. Uncertainties of the echo-sounders were 0.5% and 0.25% for moderate and more energetic sea states, respectively. The mooring load cells had an uncertainty of 0.2% for the most severe sea states.

3.2. Device scaled model

The tests of the UGEN device considered a geometrical scale of 1:24.

This scale was chosen to allow the testing in both moderate and highly energetic sea states in the wave basin.

The model geometry and mass distribution were obtained through numerical optimization, using the algorithm described in [23]. Two different floating load conditions were tested: without internal OWC and with a U-tank filled with 70 kg of fresh water, leading to two different device draughts (T_1 and T_2), which ultimately influence the resonance frequencies of the device.

Two issues changed the Centre of Gravity (CG) of the model. First, the steel structure was heavier than initially estimated by the manufacturer. Second, the equipment installed in the model was also placed at a higher position. These issues led to the need to add 200 kg of solid ballast (lead bars) at the model's bottom compartments to attain a transverse stable equilibrium condition.

The correction of the vertical position of CG led to a large heel angle to the side of the incoming waves. This effect was aggravated by filling the U-tank with fresh water. These heel angles were corrected by installing two foam blocks at the bottom of the model (a triangular wedge of 0.025 m³ and a rectangular block of 0.05 m³).

The total mass of the model ready for testing was 751 kg without the internal OWC and 817 kg with the U-tank partially filled with fresh

water. As a result, the natural roll period was about twice the initially specified value. The main physical characteristics of the model are presented in Table 1. The full-scale values are also included in the table.

Since the scale of the model (1:24) was too small to perform the tests with a turbine model [31], a calibrated orifice plate was used to simulate the turbine damping effect on the system. This type of turbine simulator provides a quadratic relation between the pressure drop and the flow rate, in this way simulating an impulse turbine. An alternative to this turbine simulator would be the use of one or more apertures covered with porous material in order to induce a laminar flow regime and, therefore, a linear pressure-drop-to-flow-rate ratio [33]. This linear relationship is typical of a Wells turbine, which was also considered in the design of this device [23]. However, since the porous material can get wet due to moisture generation and contact with the water inside the U-tank, the orifice plate was chosen instead. The orifice plate consisted of a perforated steel plate with 21 orifices, each with a diameter of 10 mm, see Fig. 4b. The characteristics of the turbine simulator are summarized in Table 2. The discharge coefficient was determined through calibration.

The model was initially instrumented with 14 strain gauges, but only 12 were operational due to damages in 2 of them, see Fig. 5.

During regular- and irregular-wave experiments, the water depth was kept constant at 2.5 m. The tests duration was set to 180 s for regular waves and 325 s for irregular waves (at model scale).

4. Results

4.1. Loading and stability

Traditionally, a transverse inclining test is performed aboard by placing an appropriate weight in a transverse offset position from the vertical axis passing through the centre of gravity of the floating body, as described in [34]. As the hull is asymmetric in the transverse plane, a longitudinal inclining test was conducted to avoid corrections associated with the transverse shift of the centre of buoyancy. The longitudinal inclination angles were measured relative to the device equilibrium position in still water. Two moving weights of mass of 4 kg have been utilized in the inclining experiment. The values of both longitudinal and transverse metacentric heights, which were obtained from the regression analysis of the experimental data points, are shown in Table 1.

Table 1
Main physical characteristics of the UGEN at model and full scale.

Scale	1:24	1:1
Length (L_n) [m]	1.225	29.4
Beam (B_m) [m]	1.013	24.3
Height (H) [m]	1.071	25.7
Without fresh water inside the U-tank		
Total mass (m_1) [kg]	751.0	10.38×10^6
Draught (T_1) [m]	0.517	12.4
Moment of inertia about x-axis [kg m^2]	119.4	0.95×10^9
Moment of inertia about y-axis [kg m^2]	153.2	1.12×10^9
Metacentric height about x-axis [m]	0.041	0.99
Metacentric height about y-axis [m]	0.132	3.17
With U-tank primed		
Total mass (m_2) [kg]	817.0	11.29×10^6
Draught (T_2) [m]	0.532	12.8
Moment of inertia about x-axis [kg m^2]	128.1	1.02×10^9
Moment of inertia about y-axis [kg m^2]	157.0	1.25×10^9
Metacentric height about x-axis [m]	0.061	1.46
Metacentric height about y-axis [m]	0.087	2.09
Heave natural period (T_{33}) [s]	1.45	7.09
U-tank OWC natural period (T_{77}) [s]	1.11	5.46

Table 2

Main characteristic of the turbine simulator used in the experimental tests.

Turbine simulator type	multi-orifice plate
Number of orifices	21
Orifice diameter [m]	0.010
Total orifice area (A_0) [m^2]	1.65×10^{-3}
Discharge coefficient (C_d)	0.65

4.2. Hydrodynamic damping

Several free-decay tests were carried out to determine the model natural damped periods of the surge, sway, roll, pitch motions, and the internal OWC. The experiments consisted of imposing an initial displacement on the corresponding model mode and then releasing it until it recovers the equilibrium position while recording the movement. Hence, the analysis of the free-decay tests considered that the motion of a given mode ξ_{ii} ($i = 1, 2, 4, 5$) is described by

$$\ddot{\xi}_{ii} + \mu_{ii}\dot{\xi}_{ii} + \mu_{ii2}|\dot{\xi}_{ii}|\dot{\xi}_{ii} + \omega_{ii}^2\xi_{ii} = 0, \quad (1)$$

where μ_{ii} is the linear damping factor ($\mu_{ii} = B_{ii}/M_{ii}$), μ_{ii2} is the quadratic damping factor ($\mu_{ii2} = B_{ii2}/M_{ii}$), ω_{ii} is the natural frequency of the i -th mode of oscillation ($\omega_{ii}^2 = K_{ii}/M_{ii}$), B_{ii} is the linear damping coefficient, B_{ii2} is the quadratic damping coefficient, K_{ii} is the linear restoring coefficient and M_{ii} is the total inertia of the system in the corresponding mode ξ_{ii} in case of pure (not coupled) modes of oscillation.

Considering that ξ_{ii}^n represents the n -th value of the consecutive local maxima and minima of the free-decay time series, and assuming constant damping, the coefficients μ_{ii} and μ_{ii2} can be determined as proposed in Ref. [35]

$$\frac{2}{T_{ii}} \ln \left(\frac{\xi_{ii}^{n-1}}{\xi_{ii}^{n+1}} \right) = \mu_{ii} + \frac{16}{3} \frac{\xi_{ii}^n}{T_{ii}} \mu_{ii2}, \quad (2)$$

where T_{ii} is the damped natural period of the oscillation between the points ξ_{ii}^{n-1} and ξ_{ii}^{n+1} . The estimation of coefficients μ_{ii} and μ_{ii2} has been performed by plotting the left hand side of Eq. (2) against $\frac{16}{3} \frac{\xi_{ii}^n}{T_{ii}}$ and adjusting a linear regression through those points [35].

The summary of results from the free-decay tests is presented in Table 3. An example of a free-decay test in the roll mode with the mooring system applied is presented in Fig. 6. The experimental measurements are compared with the analytical free-decay curve with linear damping, whose amplitudes decay in time following the function $\exp(-\omega_{44}\zeta_{44}t)$, where ζ_{44} is the damping factor in the roll mode. The equivalent linear damping coefficient is given by $B_{44}^{\text{eq}} = 2\zeta_{44}K_{44}/\omega_{44}$, assuming that the decay frequency is approximately equal to the natural frequency of the corresponding mode. The inset plot in Fig. 6 shows the linear fit used for the determination of the coefficients μ_{441} and μ_{442} from Eq. (2). The vertical and horizontal axes correspond to coefficients $(2/T_{44})\ln(\xi_{44}^{n-1}/\xi_{44}^{n+1})$ and $(16/3)\xi_{44}^n/T_{44}$, respectively.

Damping coefficients were determined using the restoring coefficient calculated from metacentric heights presented in Table 1. For roll and pitch modes, the hydrostatic restoring coefficients were obtained from the inclining test. The restoring coefficient in surge and sway were determined using the mooring restoring forces in the corresponding direction. As expected, surge and sway natural periods are much larger than roll and pitch natural periods.

4.3. Rigid body and internal OWC motions

In this experimental testing programme, only unidirectional waves were considered. Hence, due to the device symmetry about the ξ_{22} -axis,

Table 3

Results from the experimental free-decay tests at UoP COAST Lab, including dimensionless natural periods and damping coefficients of the UGEN at model and full scale in surge, sway, roll and pitch modes.

		1:24	1:1	
Surge	Dimensionless natural period, T_{11}/T_{44} [-]	7.885	7.885	
(U-tank empty)	Damping (linear), B_{11_1} [kg/s]	54.98	1.55×10^5	
	Damping (quad.), B_{11_2} [kg/m]	2.17×10^3	1.25×10^6	
	Damping (lin. eq.), $B_{11_1}^{eq}$ [kg/s]	126.2	3.56×10^5	
Sway	Dimensionless natural period, T_{22}/T_{44} [-]	8.053	8.053	
(U-tank empty)	Damping (linear), B_{22_1} [kg/s]	6.63	1.87×10^4	
	Damping (quad.), B_{22_2} [kg/m]	2.57×10^3	1.48×10^6	
	Damping (lin. eq.), $B_{22_1}^{eq}$ [kg/s]	84.9	2.40×10^5	
Roll	Dimensionless natural period, T_{44}/T_{44} [s]	1	1	
	Damping (linear), B_{44_1} [kgm ² /(srad)]	6.81	1.11×10^7	
	Damping (quad.), B_{44_2} [kgm ² /rad ²]	3.52	2.80×10^7	
	Damping (lin. eq.), $B_{44_1}^{eq}$ [kgm ² /(srad)]	24.8	4.03×10^7	
Roll	Dimensionless natural period, T_{44u}/T_{44} [-]	0.959	0.959	
(unmoored,	Damping (linear), B_{44u_1} [kgm ² s ⁻¹ rad ⁻¹]	13.2	2.14×10^7	
U-tank empty)	Damping (quad.), B_{44u_2} [kgm ² /rad ²]	2.14	1.70×10^7	
	Damping (lin. eq.), $B_{44u_1}^{eq}$ [kgm ² /(srad)]	20.3	3.30×10^7	
	Pitch	Dimensionless natural period, T_{55u}/T_{44} [s]	0.740	0.740
	(unmoored,	Damping (linear), B_{55u_1} [kgm ² /(srad)]	90.2	1.47×10^8
U-tank empty)	Damping (quad.), B_{55u_2} [kgm ² /rad ²]	0.996	7.93×10^6	
	Damping (lin. eq.), $B_{55u_1}^{eq}$ [kgm ² /(srad)]	93.8	1.52×10^8	

the waves should only be able to excite the floater's motions in sway, heave, roll and the internal OWC.

The Response Amplitude Operator (RAO), defined as the ratio between the amplitude of the displacement in a particular degree of freedom and the incident regular-wave amplitude, ξ_{ij}^a/A_w , was used to characterize the UGEN dynamic behaviour.

Three different wave amplitudes were simulated for wave periods between 20 and 100% of natural roll period, T_{44} . The wave amplitude A_w and the wave period T_w of each test were determined from a time-domain analysis of free-surface elevation, considering the average values from a set of individual waves. Wave amplitude and period are presented here in their dimensionless form A_w/L and $T_w^* = T_w/T_{44}$, respectively, where T_{44} is the device's natural roll period and L is a characteristic linear dimension of the UGEN.

Fig. 7–10 show the RAO transfer functions of sway, heave, roll and OWC inclination angle as a function of the dimensionless wave period. Tests with three different wave amplitudes are presented in these figures. All the time series analyzed have been filtered to remove high-

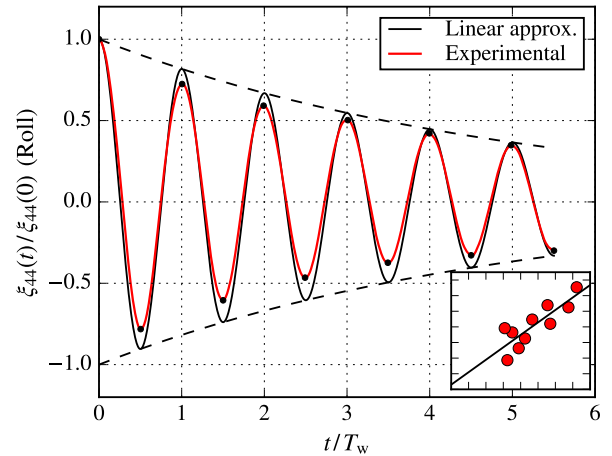


Fig. 6. Time record of a roll free-decay test with the mooring system applied and comparison with the analytical solution considering only linear damping. The inset plot was used for the determination of coefficients μ_{44_1} and μ_{44_2} described in Eq. (2), where the (red) points were determined from the time series. The line represents the best linear fit for those points using the least square method.

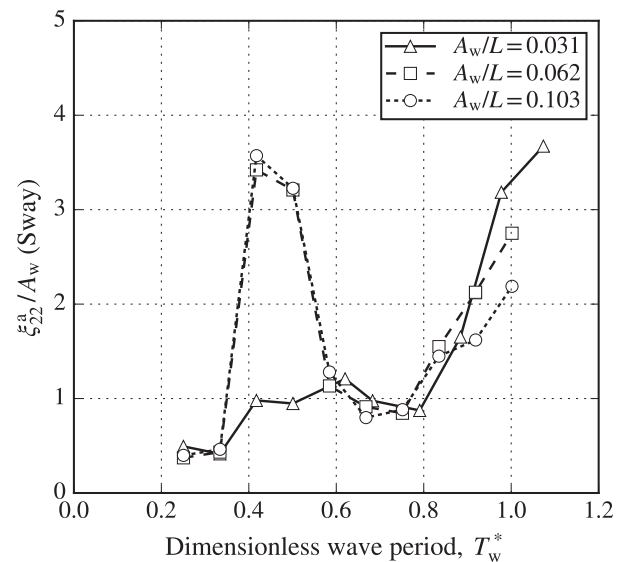


Fig. 7. Sway motion transfer function (model scale), during test runs #037 to #046, where U-tank was primed with 0.07 m³ of fresh water and regular waves were exciting the model with dimensionless periods $T_w^* = 0.2$ to 1.1 and dimensionless amplitudes of $A_w/L = 0.031, 0.062$ and 0.103.

frequency noise. For the computation of sway transfer functions, low-frequency oscillations were also filtered. The curve trends are similar in all graphs showing the coupling effects between these four oscillation modes. These couplings were also found in previous experimental tests [19]. The lowest and the highest wave periods studied ($T_w^* \approx 0.25$ and $T_w^* \approx 1$) are close to the OWC natural period and the natural roll period, respectively, and explain the trend of the graphs, showing a smaller and a much larger peak near those periods. Hence, for $T_w^* \approx 1$, the motion transfer function shows a maximum or a value very close to it. In Fig. 8, the RAO transfer function in heave also shows a peak near the heave natural period, at $T_w^* \approx 0.4$.

For the curves with $A_w/L = 0.062$ and $A_w/L = 0.103$, the RAO transfer functions of sway, heave, roll and OWC inclination angle have a peak for T_w^* varying between 0.4 and 0.5. In a region where no signifi-

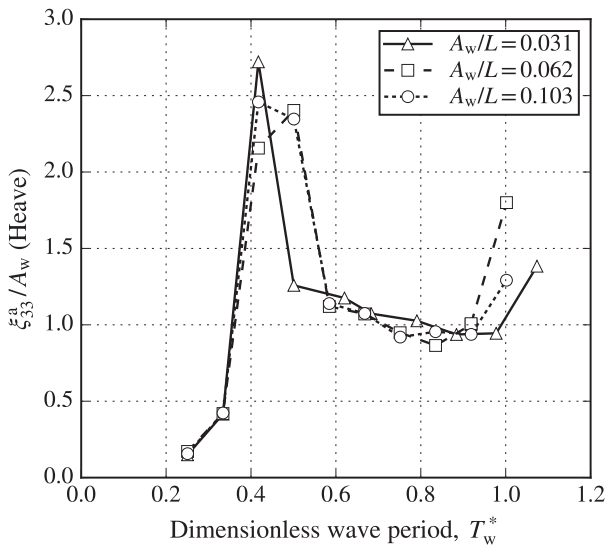


Fig. 8. As in Fig. 7, for heave.

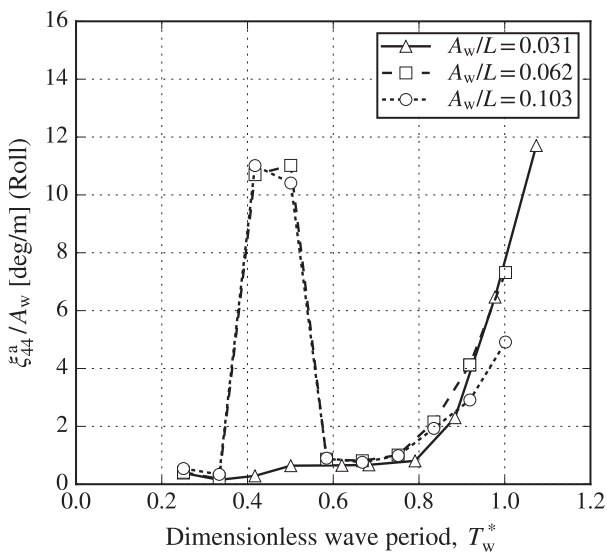


Fig. 9. As in Fig. 7, for roll. The transfer function values refer to full scale.

cant wave excitation is expected, those peaks are due to wave-induced auto-parametric resonance in the low regime. This type of resonance is a dynamic instability phenomenon that can occur due to pressure variations induced by waves on the instantaneous wetted surface or due to instantaneous variations of the hydrostatic restoring moment. This phenomenon tends to appear for wave periods around half the roll or pitch natural period (depending on the orientation of the incoming waves), and is more pronounced with increasing wave amplitudes. Furthermore, at the transient stage of parametric resonance, energy transfer among different modes is likely to occur [28,29]. Further details on WEC experiments with the observation of parametric resonance effects are found in [36,37].

To visualize transient and stationary stages of the parametric resonance, time series of two regular-wave tests with the same wave amplitude and for slightly different wave periods ($T_w^* = 0.501$ and $T_w^* = 0.585$) are presented in Fig. 11. The time intervals of the data presented in the graphs are described in Section 3.1. The test with $T_w^* = 0.585$ shows the UGEN's response to the incident wave excitation, with motion oscillations presenting a period equal to the incident wave. For the responses with $T_w^* = 0.501$, auto-parametric resonance is observed, where

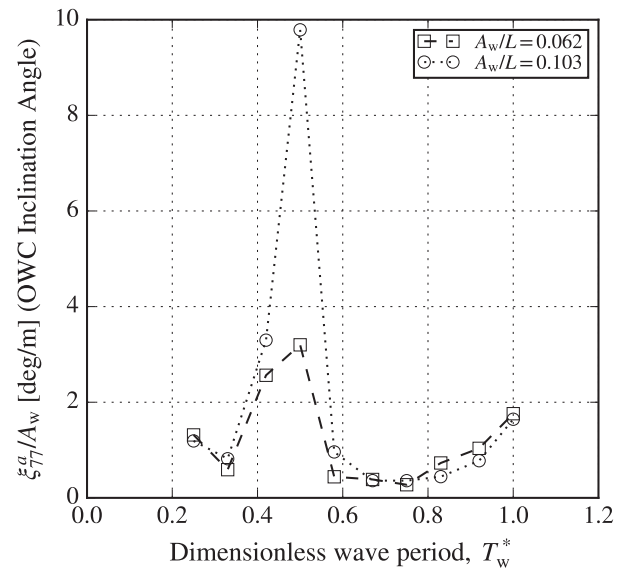


Fig. 10. As in Fig. 7, for internal OWC. The transfer function values refer to full scale.

the amplitudes of roll steadily increase on each successive cycle of the transient regime until a permanent periodic state is attained, reaching a maximum amplitude above 10 deg/m. The so-called low-cycle instability region of the auto-parametric rolling condition corresponds to a roll motion period twice the incident wave period. The pitch motion (not shown here) was practically negligible in both cases.

It is worth noting that, for $A_w/L = 0.031$, sway, roll and inclination of internal OWC modes (Figs. 7, 9 and 10) do not present any significant non-linear dynamic effect. This observation indicates that parametric resonance will only occur for amplitudes above a certain threshold, as the damping forces below those conditions are enough to dissipate auto-parametric resonance and avoid its triggering (see e.g. [28,29]). A study on the effect of the wave amplitude in the occurrence of parametric resonance of a floating OWC device can be found in Ref. [38].

The results show two significant dynamic amplification of the roll motion, one around the natural roll period and the other around the low-cycle auto-parametric resonance period. Although these periods are quite separated in the time range, both are important because rolling is the primary driving mode for wave energy extraction in the UGEN's PTO. Apart from a major peak at the low-cycle auto-parametric resonance condition, the RAO transfer function of the OWC inclination shows two peaks, one is related to the UGEN's natural damped period of roll, while the other is related to the natural damped period of the internal OWC (see Fig. 10). Moreover, the strong coupling between sway, heave, and roll modes – especially for the natural roll period – demonstrates that the UGEN can extract wave power from these modes of motion.

Fig. 12 shows the dimensionless mean value of sway displacement per unit of squared wave amplitude for three different wave amplitudes. The presence of wave drift forces explains the deviation of the average value from zero. As expected, this effect is higher for lower wave periods and tends to decrease with the increase of the wave period or as the device's dimension relative to the incident wavelength becomes smaller. Fig. 12 shows a significant drift of the model for the lower wave period. This effect is expected to vary proportionally to the wave amplitude square (A_w^2). However, this is not observed for the lower wave periods, presumably due to the non-linearities introduced by the mooring system. The variation observed at $T_w^* \approx 0.4$ is considered to be related to the interaction with other effects, namely parametric resonance.

For the analysis of displacements in irregular wave conditions, the normalized displacement factor, $\sigma_{\xi_{ih}}^*$, has been considered to compare the

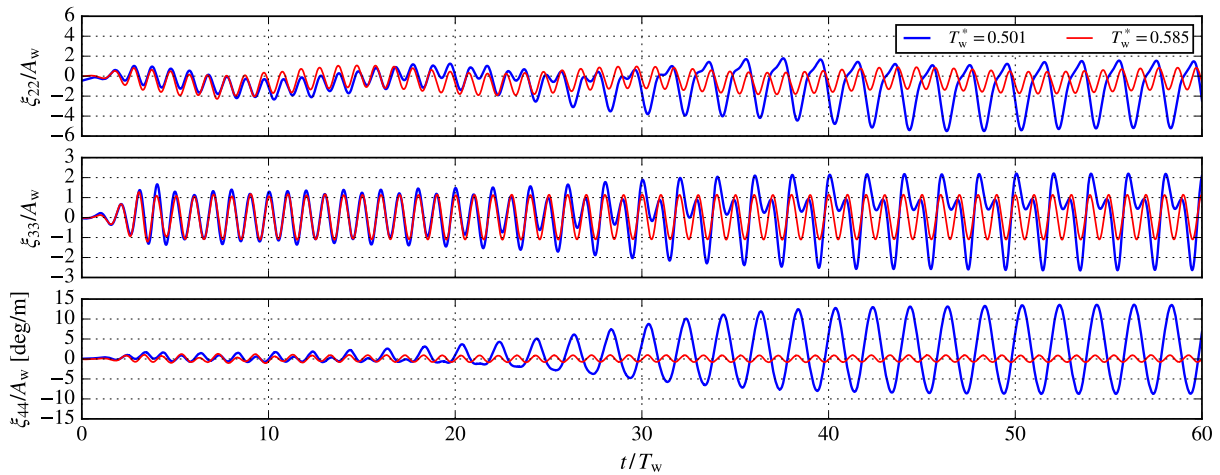


Fig. 11. Time records of dimensionless sway, heave and roll during test runs #050 and #051, where U-tank was primed and regular waves were exciting the model with dimensionless wave periods $T_w^* = 0.501$ and $T_w^* = 0.585$ while dimensionless wave amplitude was kept constant as $A_w/L = 0.062$.

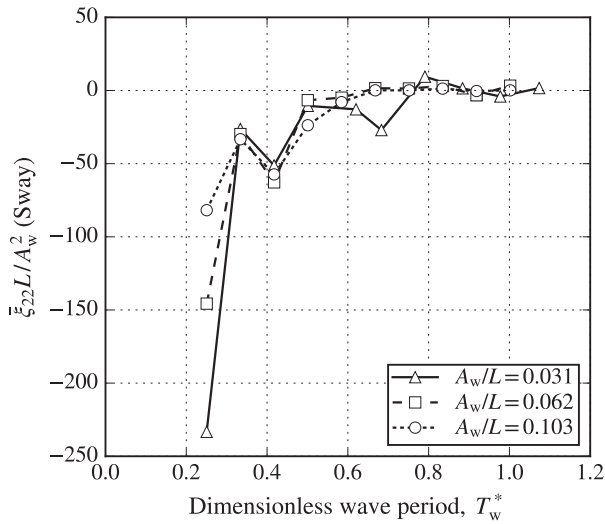


Fig. 12. Normalized average value of the sway displacement in regular waves as a function of the dimensionless wave period for three different wave amplitudes.

results for sea states with different significant wave heights. This parameter is defined as

$$\sigma_{\xi_{ii}}^* = \sigma_{\xi_{ii}} / \sigma_w, \quad (3)$$

where $\sigma_{\xi_{ii}}$ is the standard deviation of the ii -th mode ξ_{ii} and σ_w is the standard deviation of the free-surface elevation, η_w . For a Pierson-Moskowitz spectrum [39], the significant wave height is $H_s = 4\sigma_w$. The significant wave height H_s and the energy period T_e were determined using a spectral analysis [39] implemented in MatLab.

Three significant wave heights, H_s , have been considered throughout the experiments, corresponding to the dimensionless standard deviation of the free-surface elevation values $\sigma_w/L = 0.016, 0.031$ and 0.051 .

Figs. 13–15 present the normalized displacement factor of sway, heave and roll for irregular waves. The displacement signals were filtered to remove high-frequency noise and low-frequency oscillations. This filtering is particularly relevant for sway, where the displacement factor is affected by wave drifting.

Sway and roll displacement factors present distinct trends, depending on the σ_w/L value, see Figs. 13 and 15. Unlike roll and sway, heave presents an approximately linear response, as the motion is proportional

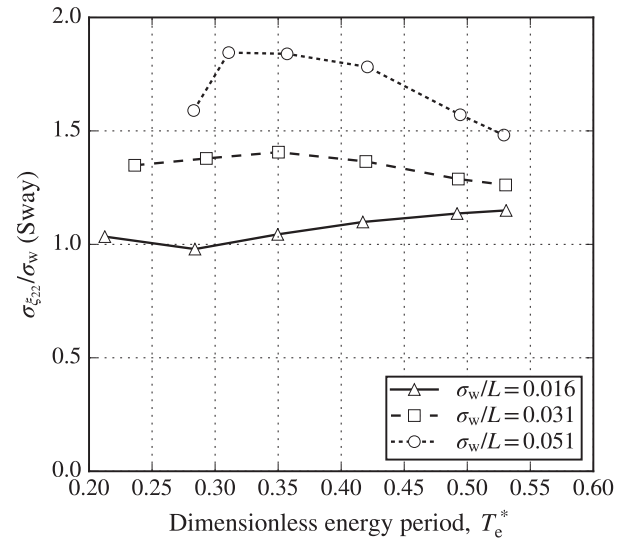


Fig. 13. Irregular-wave results of normalized displacement factor in sway as a function of the dimensionless energy period with three different values of dimensionless standard deviation of the free-surface elevation, σ_w/L .

to σ_w/L for the same value of T_e^* . All curves present a maximum value at $T_e^* \approx 0.4$, which is in close agreement with the regular wave results.

The increase of the normalized displacement factor with the σ_w/L for sway and roll indicates non-linear effects. These non-linearities are associated with low-cycle auto-parametric resonance in waves and wave drift effects, as both phenomena were identified and detected in the regular wave analysis for the range of frequencies being excited by these tested sea states. Therefore, to properly analyze the wave mean drift effect on the UGEN's motion, Fig. 16 shows the normalized average displacement of sway for the irregular waves test runs. The plot shows a large average displacement in the wave direction for the lower energy periods. This effect tends to decrease with the increase of the energy period. Finally, smaller variations in these curves result from interaction with other modes and those non-linear effects referred to previously.

4.4. Pressure difference between air chambers

A dimensionless pressure difference between the two air chambers was defined as

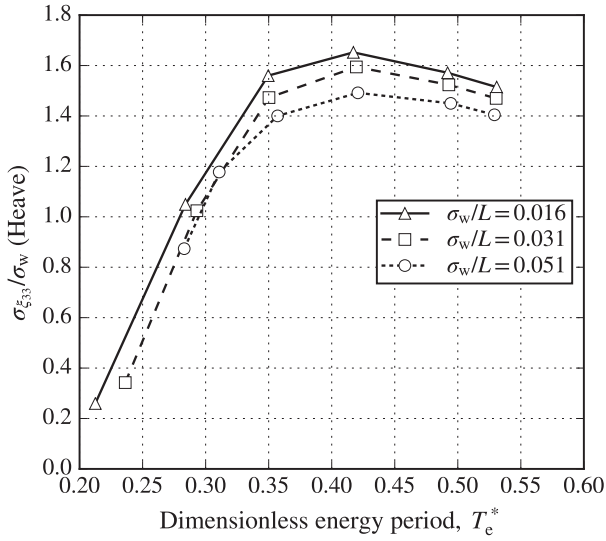


Fig. 14. As in Fig. 13, for heave.

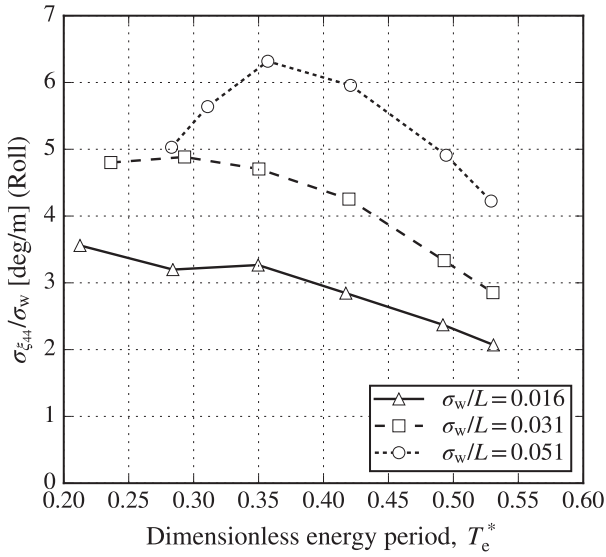


Fig. 15. As in Fig. 13, for roll.

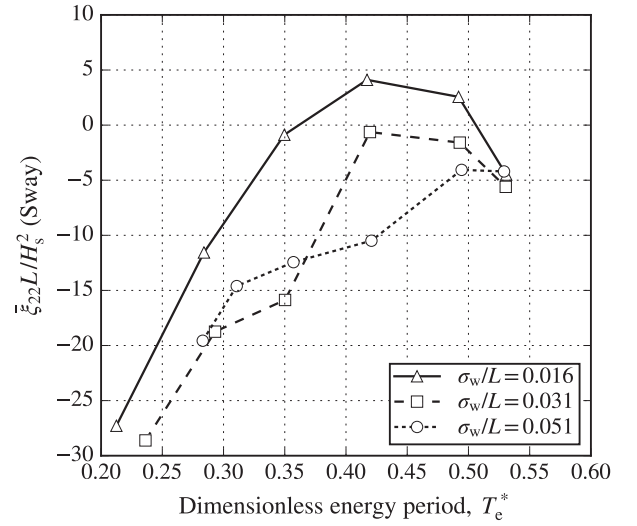


Fig. 16. Normalized average values of sway displacement in irregular waves as a function of the dimensionless energy period for three different values of σ_w .

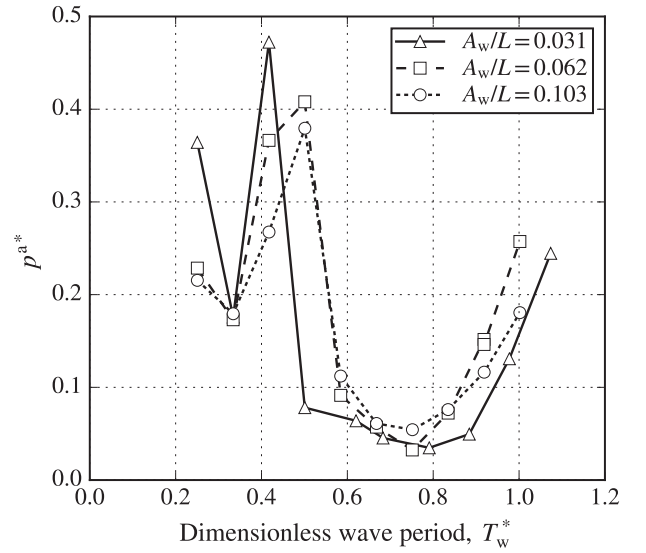


Fig. 17. Dimensionless pressure difference amplitudes from regular wave tests with different wave amplitudes.

$$p^* = \frac{p}{\rho_w g A_w}, \quad (4)$$

to compare the pressure available to the turbine as a function of the wave amplitude. Here p is the pressure difference between the air chambers, ρ_w is the water density and g is the acceleration of gravity. The pressures measured in the two chambers relative to the atmosphere have the same absolute value, but opposite signals since the two air chambers have the same volume.

Fig. 17 shows the variation of dimensionless pressure difference amplitude p^* against the dimensionless wave period T_w^* , for the three tested dimensionless wave amplitudes A_w/L . Firstly, the variation of the dimensionless pressure difference amplitude p^* with T_w^* is identical for the three-wave amplitudes tested. Next, the shape of the pressure curves shows similar trends with those of the heave transfer function (for $T_w^* < 0.6$, see Fig. 8), and those of the sway and roll transfer functions (for $T_w^* > 0.6$, see Figs. 7 and 9).

An FFT analysis of p^* has been performed for all tests to identify the most relevant frequencies. Under normal operating conditions, the regular wave-induced pressure difference is expected to have the same

frequency as the incident wave. However, in cases where the system has a non-linear behaviour, this typical linear response was not verified.

Table 4 presents the dimensionless wave period (T_w^*) and the dimensionless periods of the highest components of the pressure

Table 4

Identification of the two most relevant components of the pressure different response from regular wave tests with $A_w/L = 0.062$.

T_w^*	$T_{p(1)}^*$	$p_{(1)}^*$	$T_{p(2)}^*$	$p_{(2)}^*$
0.25	0.25	0.176	0.13	0.023
0.34	0.33	0.188	0.17	0.004
0.42	0.42	0.276	0.85	0.266
0.50	0.50	0.091	1.02	0.216
0.58	0.58	0.083	0.39	0.006
0.66	0.66	0.047	0.34	0.007
0.76	0.76	0.032	0.38	0.012
0.85	0.85	0.063	0.42	0.009
0.93	0.93	0.114	0.45	0.007
1.02	1.02	0.197	0.50	0.006

response ($T_{p(1)}^*$ and $T_{p(2)}^*$) and their corresponding dimensionless amplitudes ($p_{(1)}^{a*}$ and $p_{(2)}^{a*}$) for each test with $A_w/L = 0.062$. The dimensionless period $T_{p(1)}^*$ is equal to each test's wave period. In most tests, $p_{(1)}^{a*}$ is much higher than $p_{(2)}^{a*}$, indicating that the dominant excitation occurs at the same frequency as the wave frequency. Since $T_{p(1)}^* \approx 2T_{p(2)}^*$, it can be inferred that the pressure amplitude of the second component ($p_{(2)}^{a*}$) is a result of a higher order mode excitation. However, for $T_w^* = 0.42$ and $T_w^* = 0.50$, corresponding to tests where parametric resonance was identified, $p_{(2)}^{a*}$ is comparable to, or higher than, $p_{(1)}^{a*}$, and $T_{p(1)}^* \approx \frac{1}{2}T_{p(2)}^*$.

The results from Table 4 show that auto-parametric resonance have a strong effect on the pressure difference between the two air chambers for T_w^* between 0.4 and 0.5 and $A_w/L = 0.062$. Comparing tests with $A_w/L = 0.062$ and $A_w/L = 0.103$ (under low-cycle auto-parametric resonance) and tests with $A_w/L = 0.031$ (no auto-parametric resonance), it is clear that the pressure difference amplitudes are higher under ideal synchronisation between waves and low-cycle auto-parametric resonant roll responses at $T_w^* \approx 0.5$ and lower at $T_w^* \approx 0.4$. However, from the results shown in Table 4, it is not possible yet to ascertain whether its overall effect will always be advantageous in terms of energy extraction from waves compared with a WEC UGEN working under pure resonant conditions in beam waves.

Finally, since the range of periods tested in these experiments did not include the natural damped sway frequency, no direct excitation of the OWC could be observed in this mode.

For the analysis of the pressure difference between the two lateral air chambers in irregular waves, the dimensionless standard deviation of the pressure difference is

$$\sigma_p^* = \frac{\sigma_p}{\rho_w g \sigma_w} \quad (5)$$

where σ_p is the standard deviation of the pressure difference between the two lateral air chambers.

Fig. 18 shows the variation of σ_p^* with the energy period for tests in irregular waves considering different values of the dimensionless standard deviation of the free-surface elevation. The curves for different σ_w/L display an overlapping, suggesting that the pressure difference between air chambers is, in fact, proportional to σ_w/L (or H_s) even though the turbine simulator utilized during the tests have a non-linear characteristic. Considering that the pressure difference is a quadratic

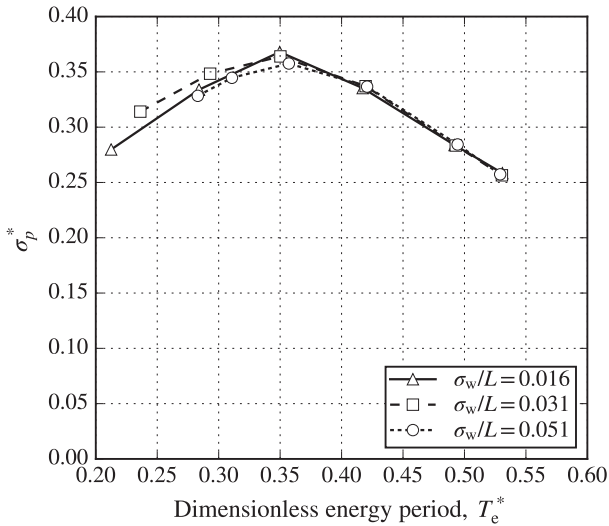


Fig. 18. Dimensionless pressure difference standard deviation in irregular waves as a function of the dimensionless energy period with three different values of dimensionless standard deviation of the free-surface elevation $\sigma_w/L = 0.016, 0.031$ and 0.051 .

function of the volume flow rate for a perforated disk with circular orifices (see Eq. (8)), the instantaneous power available to the turbine should be proportional to the pressure difference to the power of 3/2.

The characteristics of the turbine simulator of the UGEN's 1:24th-scale model are presented in Table 2, where the discharge coefficient, C_d , was determined through experimental calibration.

4.5. Power extraction

The model's power extraction efficiency is determined using the Capture Width Ratio (CWR). As in Ref. [18], this parameter is defined as the ratio between the time-averaged absorbed power by the converter \bar{P} , and the energy flux per unit wave crest length, \bar{P}_w , times the width of the device, L_n , which is given by

$$\text{CWR} = \frac{\bar{P}}{L_n \bar{P}_w} \quad (6)$$

The value of \bar{P}_w was determined from the free-surface elevation measurement by taking into account the water depth effect [40].

The time-averaged power dissipated by the perforated disk between the time instants t_i and t_f is given by

$$\bar{P} = \frac{1}{t_f - t_i} \int_{t_i}^{t_f} p Q dt, \quad (7)$$

where Q is the volumetric flow rate passing through the turbine simulator as given by

$$Q = C_d A_0 \sqrt{\frac{2}{\rho_a} |p|^{-\frac{1}{2}} p}. \quad (8)$$

Here C_d is the orifice plate's discharge coefficient, ρ_a is the air density, and A_0 is the area covered by the orifices. The characteristics of the 90 mm diameter perforated disk are given in Table 2.

Fig. 19 presents the CWR as a function of the dimensionless wave period for all regular wave tests. The CWR presents a peak for $T_w^* \approx 0.4$, as in Fig. 17 for the pressure difference amplitude, and its value is low for $0.6 < T_w^* < 0.9$. The power extraction seems to be more efficient for the lower wave amplitude ($A_w/L = 0.031$), with a peak at $T_w^* \approx 0.25$, corresponding to the OWC natural period. However, after low-pass filtering, this value has been significantly reduced, indicating that this particular data point's accuracy should be further investigated. The peak

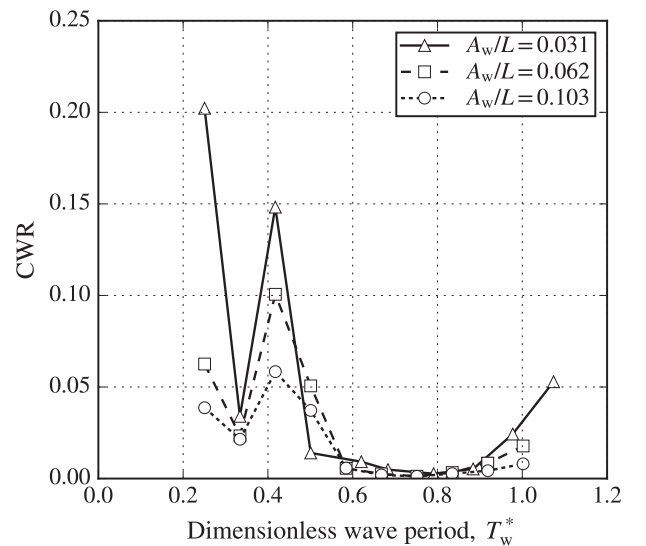


Fig. 19. Capture Width Ratio (CWR) of the UGEN in regular waves with three different dimensionless wave amplitudes $A_w/L = 0.031, 0.062$ and 0.103 .

at $T_w^* \approx 0.4$, near the natural heave period, also displays a significant efficiency in terms of power extraction. Finally, the curves for $A_w/L = 0.062$ and 0.103 are above the curve for $A_w/L = 0.031$ at $T_w^* \approx 0.5$, showing that low-cycle auto-parametric resonance is producing a positive effect in terms of power extraction from waves for this wave period.

Fig. 20 shows the capture width ratio for irregular waves. For the range of energy periods that have been tested, CWR decreases with the increase of the energy period. The curves plotted in Fig. 20 exhibit the same trend shown in Fig. 19, in particular at the shortest wave periods where the energy flux per unit wave crest length is considerably lower than for larger wave periods (see Eq. (6)). Therefore, the decrease of CWR with the increase in the values of the dimensionless standard deviation of the free-surface elevation σ_w/L is not surprising.

4.6. Mooring system

It is advantageous not to restrict sway, heave and mainly roll movements to maximize UGEN's power extraction, but it is imperative to use moorings to attenuate surge, pitch and yaw and keep the device on station. Throughout the experiments, the wave incidence angle was kept constant, and the forces on the mooring lines were measured using load cells intercalated on each mooring line. Three mooring lines have been installed as shown in Fig. 1b. As expected due to symmetry, loads at mooring lines ML#1 and ML#2 are very similar. Therefore, only results of ML#1 and ML#3 are presented here. For regular waves, the dimensionless mooring tension is defined as

$$f^* = \frac{f}{\rho_w g S_{wp} A_w}, \quad (9)$$

where f is the tension measured by the load cell and $S_{wp} = L_n B_m$ is the device waterplane area. For this analysis, the pre-tension of the lines, f_0 , was considered, whose value was measured under still water conditions.

Fig. 21 shows a statistical summary of the line tension measured under regular-wave excitation conditions. These graphs display the load values distribution as a function of the dimensionless wave period for two distinct wave amplitudes ($A_w/L = 0.031$ and 0.103), where density trace, median, extrema and quartiles of those distributions are all identified in the caption.

Fig. 21 exhibits a median of $f^* - f_0^*$ displaced from zero for ML#1 and ML#3 under lower wave periods, indicating the presence of wave drift effects. Moreover, with the increase of the wave period, the median

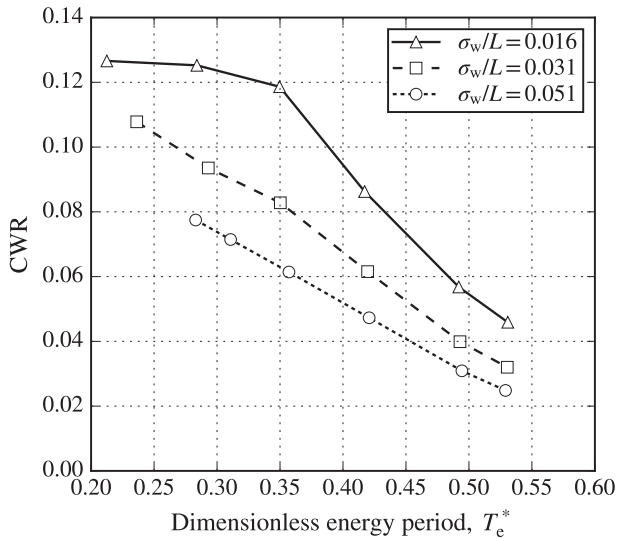


Fig. 20. Capture Width Ratio (CWR) of the UGEN in irregular waves as a function of the dimensionless energy period with three different standard deviation of the free-surface elevation $\sigma_w/L = 0.016$, 0.031 and 0.051 .

tends to zero in all cases, showing the expected decrease of wave drift effects at these lower wave frequencies. The non-linear characteristic of wave drift effects is also noticeable since the load variation on the ML#1 per wave amplitude is much more significant for the case with $A_w/L = 0.103$ than for the case with $A_w/L = 0.031$. It can be also inferred that the highest peaks and variations in line tension are observed for $T_w^* \approx 0.25$ and $T_w^* \approx 0.4$. Moreover, for $T_w^* \approx 0.25$, the loads are caused by wave drift effects due to the device's horizontal excursion, and the highest peak occurs on ML#1 for $A_w/L = 0.103$.

For $T_w^* \approx 0.4$, the mooring loads are now induced not only by wave drift effect but also by the so-called low-cycle auto-parametric resonance effect mentioned before. Due to large coupled sway-roll motion amplitudes under parametric rolling, the loads on ML#3 are now significantly higher in this particular resonant condition. The load variations are low for the other range of dimensionless wave periods, yet relatively higher values are again observed near the natural roll period ($T_w^* \approx 1$).

All modes affect the mooring loads, but sway is noticeably the most relevant. Fig. 22 presents the time records of sway and mooring load for two regular-wave tests with $T_w^* = 0.501$ and $A_w/L = 0.031$ and 0.103 . For the case with $A_w/L = 0.031$, the sway response exhibits moderate displacements, and two frequencies are found in the plot: the wave frequency and a lower frequency. Both frequencies are visible in the time series of the loadings on ML#1.

For the case with $A_w/L = 0.103$, the sway response is affected by low-cycle auto-parametric resonance. After the initial cycles, the sway response changes, and auto-parametric rolling builds up, increasing each successive swing's amplitude up to the steady-state regime's amplitude. A similar effect is observed in the time record of the ML#1 load.

For the analysis of the mooring lines in irregular waves, the dimensionless mooring line tension is defined by

$$f^* = \frac{f}{\rho_w g S_{wp} \sigma_w}. \quad (10)$$

Fig. 23 presents distributions of the dimensionless mooring line tension ($f^* - f_0^*$) measured in irregular waves for dimensionless standard deviation of the free-surface elevation of $\sigma_w/L = 0.016$ and 0.051 . Similarly to regular waves, the median of the tension values in irregular waves tend to the pre-tension value with the increase of T_e^* . This increase is a consequence of the wave drift effect presented in Fig. 16. For the lower energy periods, the median of ML#1 presents values higher than the pre-tension f_0^* , as the average excursion in sway increases the mooring line's extension.

For low energetic sea states, such as $\sigma_w/L = 0.016$, the tension on mooring line ML#3 presents higher variations than in the line ML#1. These variations result from the wave drift effects being small for $\sigma_w/L = 0.016$, allowing other effects to become more relevant. The mooring line ML#3 lies aligned with the incident wave direction, whereas line ML#1 projection in the horizontal plane forms an angle of 60 deg with the direction of the incident wave. Tests with $\sigma_w/L = 0.051$ show larger displacements of the median value in comparison with tests of $\sigma_w/L = 0.016$ since wave drift effects are more severe, as it is shown in Fig. 16. Also in these tests, larger variations of the dimensionless tensions are observed for line ML#1 for $T_e^* < 0.45$. The higher values of tension were observed ($f^* - f_0^* \approx 0.08$) for the lower energy periods, which are likely to occur due to the high extension of the mooring lines ML#1 and ML#2. The results indicate that an increase of the significant wave height (or σ_w), and therefore wave drift effects, induces an average displacement of the device in the wave direction, making mooring lines ML#1 and ML#2 more exposed to high loads, particularly for the sea states with lower energy periods.

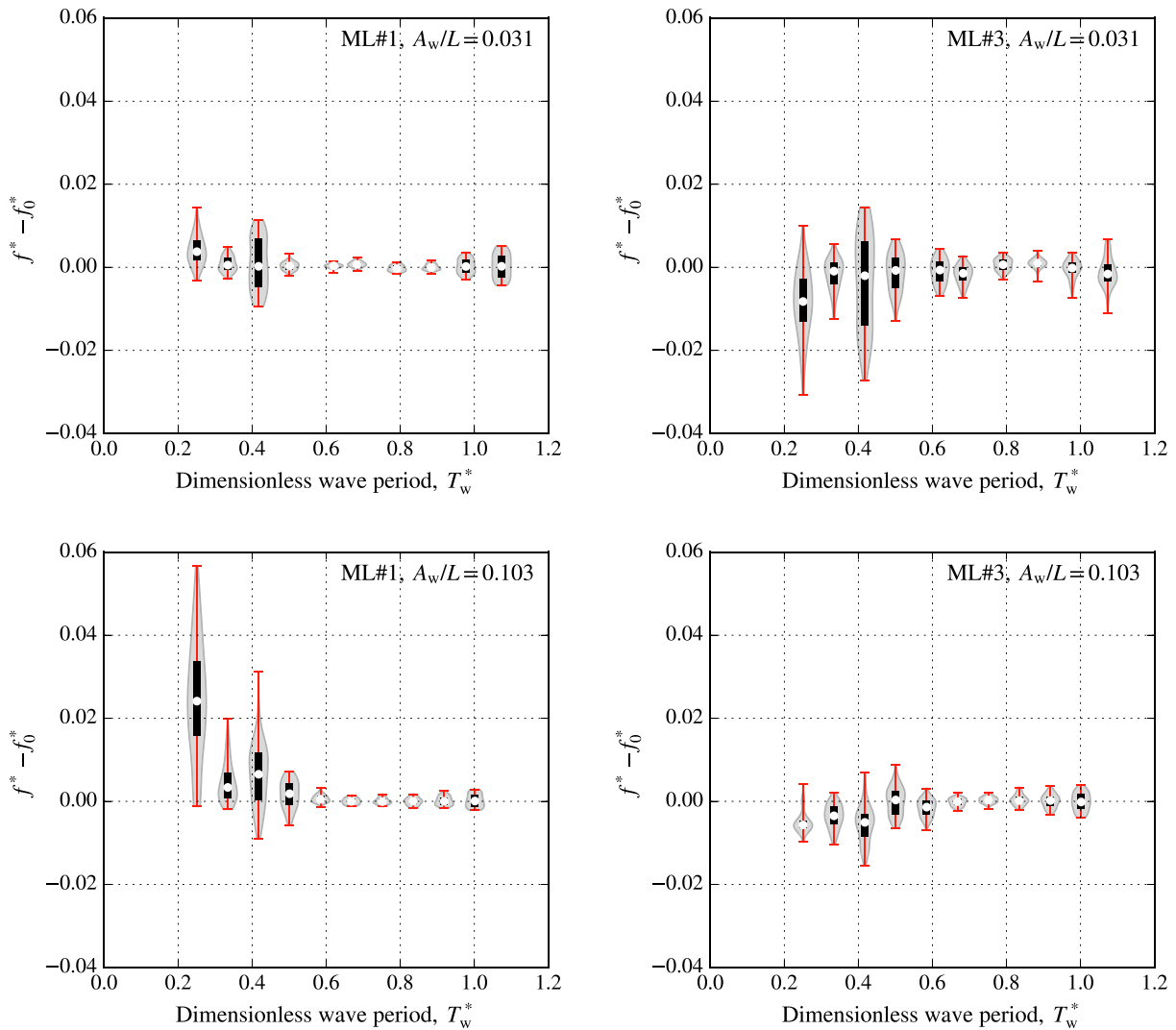


Fig. 21. Statistical summary of dimensionless mooring loads distributions in regular wave with two distinct dimensionless wave amplitudes $A_w/L = 0.031$ and 0.103 . Results for ML#1 and ML#3 are presented. Bottom and top horizontal red lines represent the extrema, the vertical thick black line shows the range of the second and third quartiles and the white point indicates the median. Grey area shaped as violin corresponds to density trace.

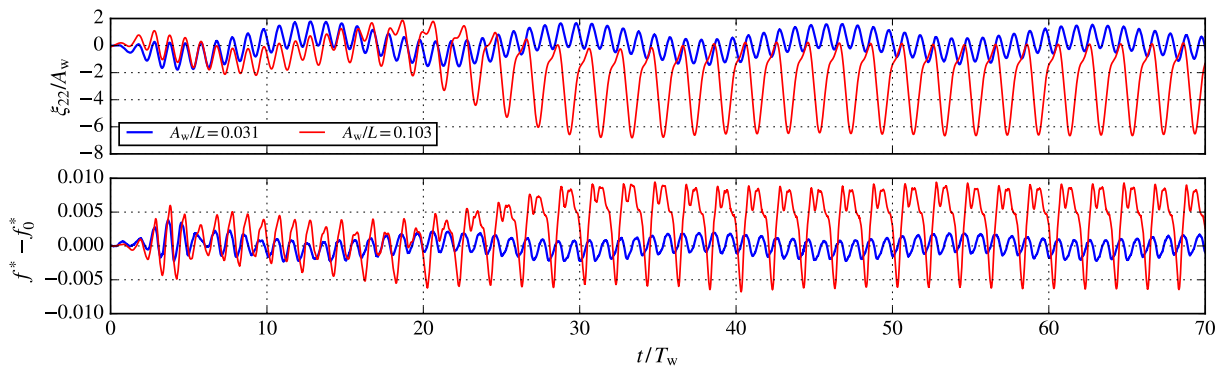


Fig. 22. Time record of motion in sway and tension at ML#1 for dimensionless wave period $T_w^* = 0.501$ and dimensionless wave amplitudes $A_w/L = 0.031$ and 0.103 .

4.7. Structural stress

The knowledge of the stress distribution on the hull is fundamental for the mechanical design of UGEN. For this purpose, 14 strain gauges were used to measure the load stresses σ of UGEN's model during the

tests. The measurements of the strain gauges present the variation of strain relative to the initial state, defined as the instant where all strain gauges have been set to zero just before the model has been deployed in the wave tank.

Fig. 24 depicts a statistical summary of stresses at the hull locations

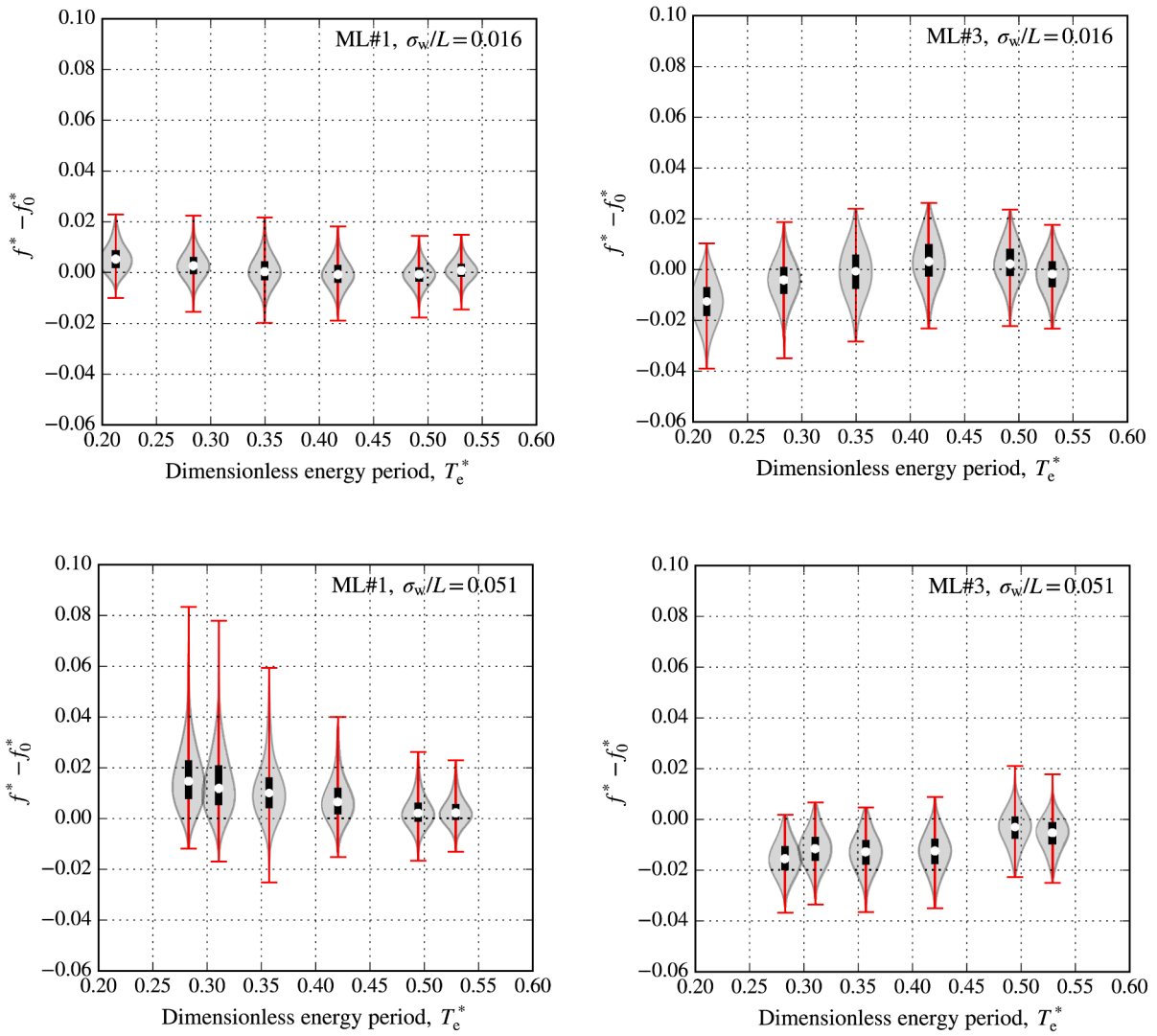


Fig. 23. As in Fig. 21, in irregular waves for $\sigma_w/L = 0.016$ and 0.051 .

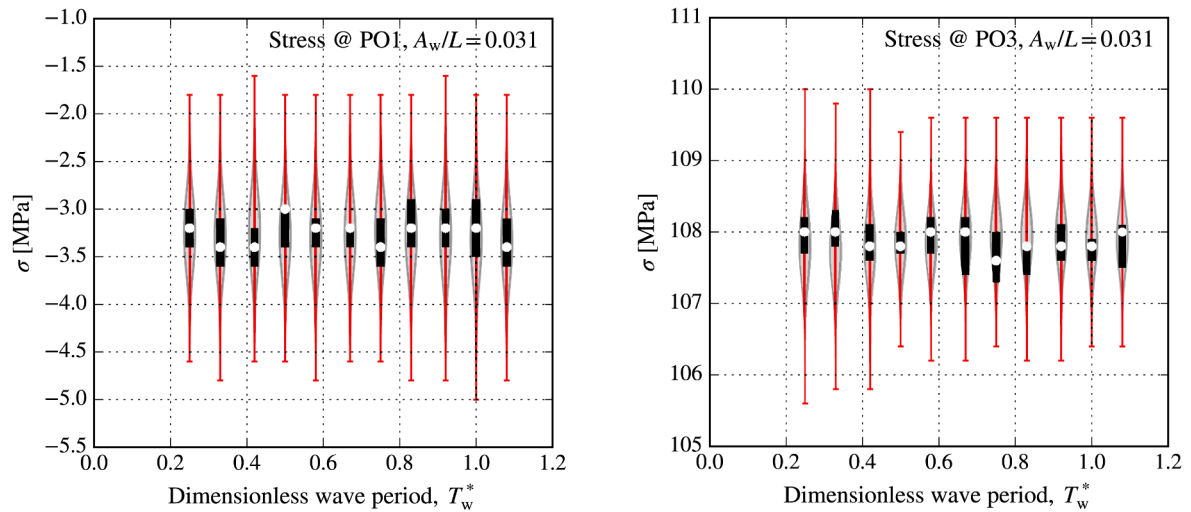


Fig. 24. Statistical summary of stress levels as a function of the dimensionless wave period (T_w^*) at two different locations (1 and 3) of the portboard side (P) taken from measurements of the outside (O) fibres of the hull plating. The horizontal red lines indicate the extrema and the grey area represents the density distribution.

PO1 and PO3 in the configuration without the U-tank primed, see Fig. 5. The plots refer to regular waves of amplitude $A_w = 0.031$ m. The results are almost independent of the dimensionless wave period in terms of average, maximum and minimum stress levels. At PO2, where the waves' effect is more relevant, the average, maximum and minimum stress levels increase with the wave period, although the plotted variance is small.

Fig. 25 shows a plot of the membrane stresses (computed as the average of the outer and inner fibre stresses) and the bending stresses (evaluated as half of the difference between the inner and outer fibre stresses). The membrane stresses at P1 and bending stresses at P3 are almost negligible compared to the membrane stress levels at P3. P3 is located well below the waterline, and the stress level increases at the hull's outer fibres to levels above +100 MPa but with a very low standard deviation, less than 2%. Notice should be given that a high level of stresses at P3 is a direct consequence of ballast weights addition after strain gauges have been set to zero.

The variation of the stress levels is small for all analyzed points, which means that the waves have not affected stress levels at those locations. Fig. 26 depicts time series of bending and membrane stresses for regular waves with $T_w^* = 0.42$ and 1.0. These plots reinforce the conclusion that regular waves do not affect much stress levels measured

at the UGEN's hull. The only regions that suffer the effect of the wave-induced loads are the ones near the waterline and the flat bottom hull plating.

4.8. Survivability tests

One of the challenges of wave energy converters is the capability to survive in highly energetic sea states. Two survivability tests were performed to evaluate the UGEN's behaviour under extreme wave conditions. These tests considered typical conditions of a North Atlantic location with similar H_s but with different energy periods ($T_e = 11.36, 12.08$ s). In this section, all values are presented at full scale. Table 5 presents the parameters of the sea states considered for the survivability tests. A Pierson-Moskowitz energy density spectrum was adopted to simulate the two sea states.

Table 6 presents a summary of the motion analysis for the two survivability tests. Only the most relevant modes are shown, i.e., sway, heave and roll. Both tests (A, B) display similar results due to the small difference in energy period, with slightly higher displacements for test A. Sway presents large displacements, especially in the wave's direction, reaching a maximum of about 42 m relative to the initial position, likely to be caused by the wave drift effect. The standard deviation values for

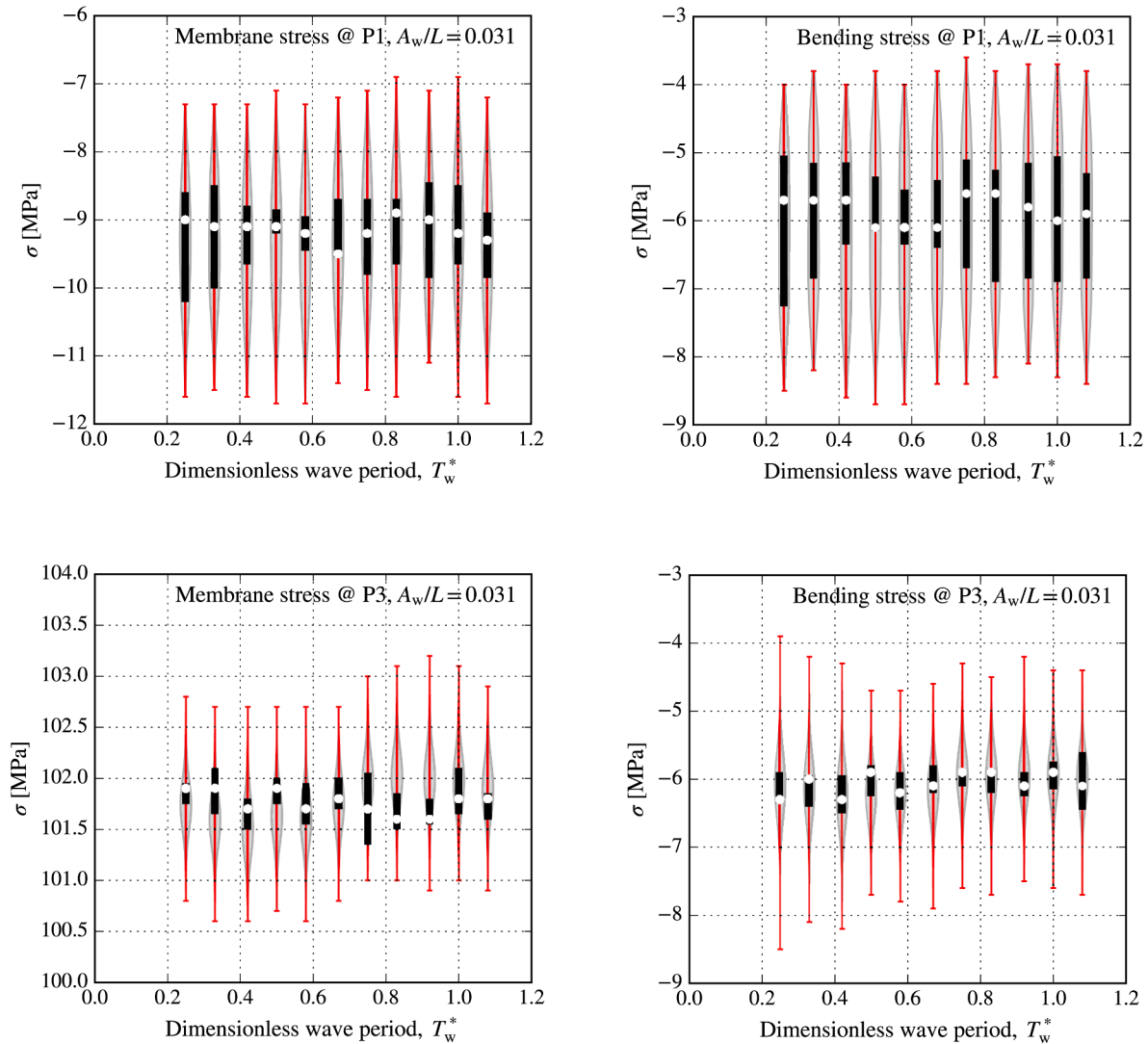


Fig. 25. Statistical summary of membrane and bending stresses at gauges P1 (top row) and P3 (bottom row) considering the exact same range of dimensionless wave periods (T_w^*) as in Fig. 24.

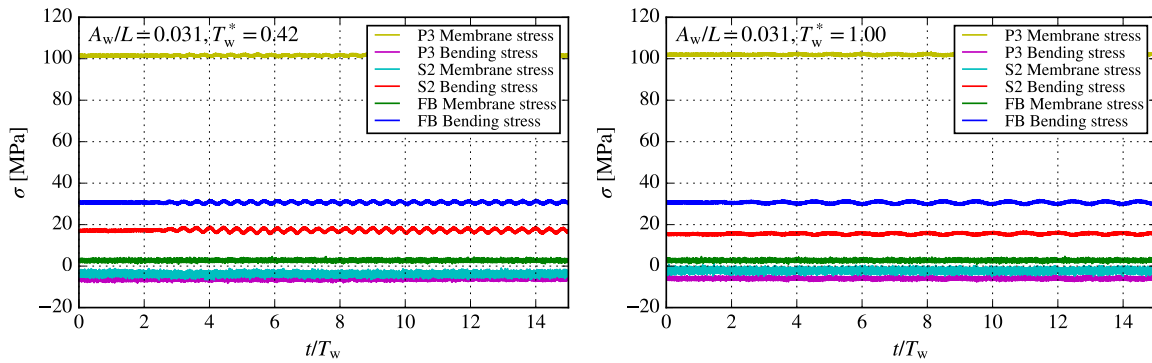


Fig. 26. Time records of bending and membrane stresses at three different locations for two distinct dimensionless regular wave periods $T_w^* = 0.42$ and 1, for two dimensionless wave amplitudes $A_w/L = 0.031$ and 0.062.

Table 5

Parameters of the sea states considered for the two survivability tests. Both tests were generated based on a Pierson-Moskowitz energy density spectrum. Values presented refer to full scale.

Test	T_c [s]	H_s [m]	$H_{1/3}$ [m]	H_{max} [m]	σ_w/L
A	11.36	8.61	7.52	14.47	0.073
B	12.08	8.72	7.48	15.50	0.074

Table 6

Results of floater motion in sway (ξ_{22}), heave (ξ_{33}) and roll (ξ_{44}) from the survivability tests. The standard deviation of mode ξ_{ii} ($\sigma_{\xi_{ii}}$), maximum ($\max(\xi_{ii})$) and minimum ($\min(\xi_{ii})$) displacement values of ξ_{ii} , and maximum height ($H(\xi_{ii})$) of the ξ_{ii} oscillations are presented. Values refer to full scale.

	A			B		
	Sway ξ_{22} [m]	Heave ξ_{33} [m]	Roll ξ_{44} [deg]	Sway ξ_{22} [m]	Heave ξ_{33} [m]	Roll ξ_{44} [deg]
$\sigma_{\xi_{ii}}$	4.22	3.25	13.05	4.30	3.02	12.77
$\max(\xi_{ii})$	-0.48	10.46	48.99	0.12	9.49	48.31
$\min(\xi_{ii})$	-42.35	-9.21	-29.78	-38.87	-8.42	-31.98
$H(\xi_{ii})$	24.06	17.46	73.80	23.01	17.50	72.00

sway and heave are similar and smaller than the corresponding roll value. Roll also shows very large displacements, with a maximum value of an individual oscillation close to 74deg.

A summary of the loads measured in the mooring lines is presented in Table 7. Results show pre-tension values, the standard deviation of load measurement and the five highest load peaks for ML#1, ML#2 and ML#3. Pre-tension shows small differences between the windward lines

Table 7

Values of load measured in the three mooring lines (f_1, f_2, f_3) during the survivability tests (A, B). The load values are in MN and refer to full scale. Line pre-tension ($f_{0,i}$), standard deviation (σ_{f_i}) and the five highest peaks measured ($\max(f_i)$).

	A			B		
	ML#1	ML#2	ML#3	ML#1	ML#2	ML#3
$f_{0,i}$	0.68	0.68	0.64	0.68	0.68	0.64
σ_{f_i}	0.30	0.30	0.14	0.23	0.22	0.15
$\max(f_i)$						
1st	2.87	2.80	0.83	2.18	2.26	0.84
2nd	2.59	2.53	0.80	1.85	1.87	0.80
3rd	2.21	2.10	0.80	1.81	1.83	0.80
4th	2.06	2.09	0.79	1.78	1.64	0.79
5th	1.93	1.92	0.76	1.75	1.64	0.79

(ML#1 and ML#2) and the leeward line (ML#3). The standard deviation of loads and peak values in the windward lines are higher than in leeward, as expected due to the wave drift effect. Despite the similarities in motion values presented in Table 6 between the two sea states, the loads measured in ML#1 for sea state A are much higher than for sea state B. This discrepancy is observed for the standard deviation and the five highest peaks. For ML#3, both sea states show similar values.

Fig. 27 presents the time series of free surface elevation, sway, heave, roll and mooring lines loads (ML#1 and ML#3) for sea state A. The five highest load peaks measured in ML#1, whose values are presented in Table 7, are indicated by the vertical lines. Wave drift effects are evident in the time series of sway (ξ_{22}). These effects generate a mean displacement and low-frequency oscillations, as observed in the plot. The low-frequency oscillations present an oscillatory period much larger than the incident wave. From the load and sway time series analysis, it is clear that the highest load peaks in ML#1 appear when the sway low-frequency oscillation reaches the largest displacement from the initial floater position, and therefore the largest extension of the ML#1. For the five peaks showed, two pairs of peaks occur after consecutive waves.

The roll motion does not seem responsible for generating very high loads on the lines, even though it endures very extreme oscillations. Time series shows that roll presents an oscillation period about twice the average period of individual waves. This observation suggests that low-cycle auto-parametric resonance is also induced in irregular waves.

A more detailed analysis of the time series presented in Fig. 28 in the vicinity of the top five load peaks identified for ML#1 would reveal that UGEN's heave response is the most important for the occurrence of the peak at those exact time instants. In fact, during the occurrence of those five peaks, heave presents a large variation, with the floater always moving upwards towards an increasing line extension so that the load peak instant in ML#1 appears about halfway through this upwards displacement when the velocity is maximum. In all five cases, the roll motion does not seem to influence the occurrence of the highest load peaks. Results demonstrate good performance of the three lines slack-mooring configuration devised for the UGEN station keeping system.

4.9. Submergence tests

Still, water preliminary tests were conducted to check whether it was possible to sink the UGEN's model at approximately the design submergence depth of 1.25 m in a controlled manner. These tests were successful in confirming that ballasting and de-ballasting procedures worked properly, and the device returned to its initial floating position as expected, see Fig. 3.

The submergence test at sea state B lasted only 2 min as the device become unstable in this position. The model started to pitch under the influence of exciting waves, changing the equilibrium position of the OWC and inducing more roll until it lay down on its windward side.

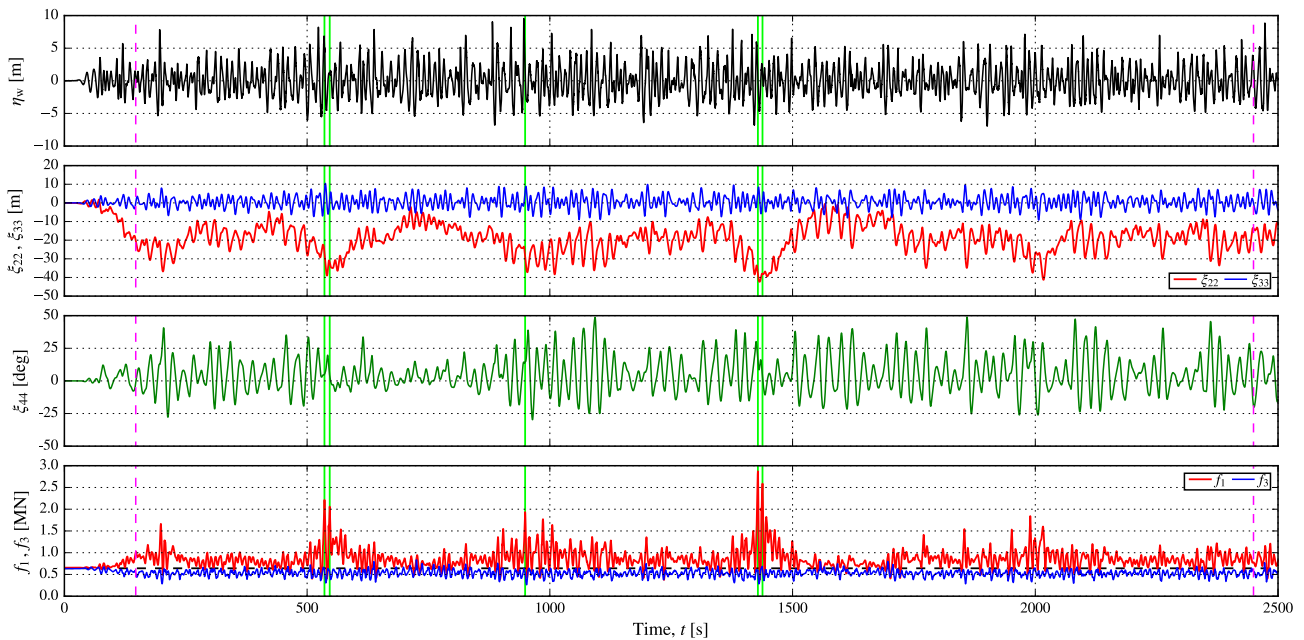


Fig. 27. Time series of free surface elevation (η_w), sway (ξ_{22}), heave (ξ_{33}), roll (ξ_{44}), ML#1 tension (f_1) and ML#3 tension (f_3), for survivability test A ($T_c = 11.36$ s and $H_s = 8.61$ m). Values refer to full scale. Vertical dashed lines indicate the initial and final instants considered for the time series analysis. The vertical solid lines indicate the instants of the five highest load peaks measured in ML#1.

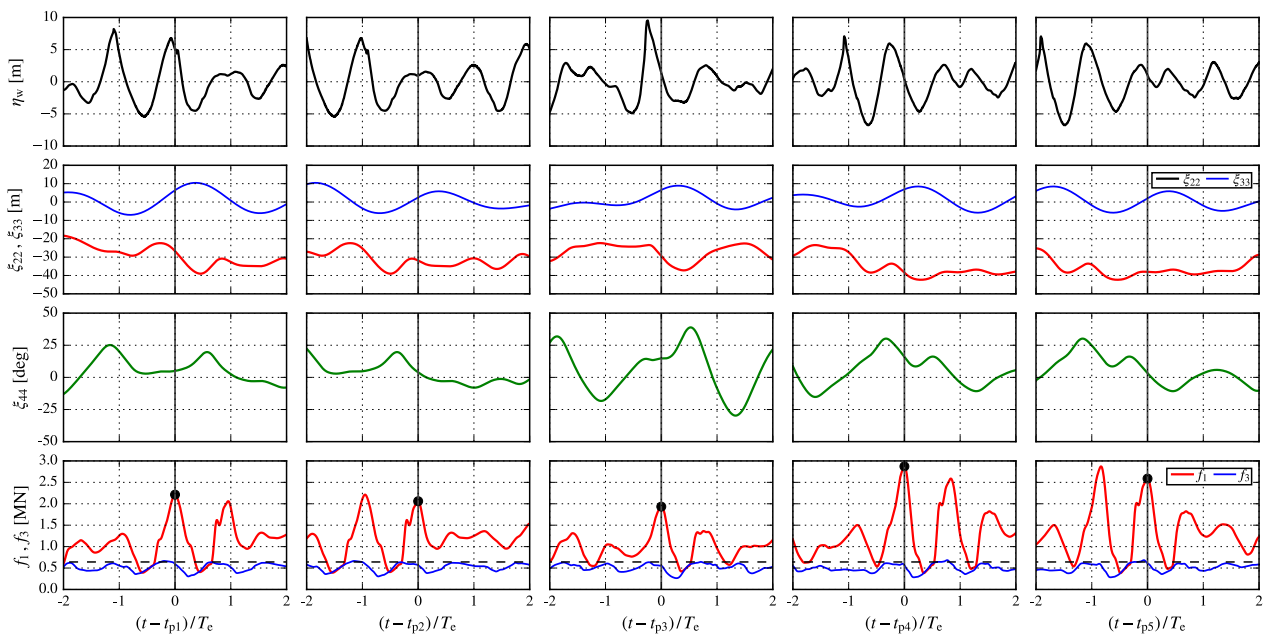


Fig. 28. Detailed view of the time series presented in Fig. 27 in the regions near the instants of the five highest peaks measured in ML#1 (graphs are organized in order of appearance in the time series). In the horizontal axis, time is relative to the instant of the n -th peak (t_{pn}) and normalized using the energy period T_c . The horizontal dashed line represents ML#1 pre-tension and the point indicates the load peak.

5. Conclusions

A 1:24th-scale model of a bottom-moored floating wave energy device with an internal U-shaped OWC – designated UGEN – was experimentally tested to assess the device performance under operational and extreme wave conditions.

The UGEN’s main driving mode for wave energy extraction is the roll motion, and regular-wave tests showed three frequencies of significant dynamic amplification of the roll motion: a) the natural damped roll period, b) the parametric resonance period, and c) the OWC natural

oscillation period.

The device testing allowed experimental confirmation of the occurrence of the low-cycle auto-parametric resonance for the first time. Moreover, there is a strong coupling between sway, heave, and roll modes, especially for the natural roll period, meaning that the device can extract wave power from these modes of motion.

Experimental results under irregular waves exhibited the same trends as the regular wave tests and also allowed detection of parametric resonance in waves. However, due to the non-linear characteristics of the turbine simulator utilized, it was not possible to determine the extent

to which parametric resonance positively affects the capture width ratio. Nevertheless, it was observed that this non-linear phenomenon could significantly improve the UGEN's overall energy conversion efficiency.

The analysis of the mooring lines tension showed that wave drift forces and parametric resonance induced important loads. Parametric resonance also induced meaningful stress levels over time, especially at the starboard side, where windward lines have been attached to the hull plating. Hence, these measurements on wave-induced structural and mooring loads are helpful to validate numerical models and cost estimates. Survivability tests showed that a combination of large horizontal displacements caused by a slow-drift motion and a large vertical excursion generated the highest load peaks on the mooring lines.

The submergence operations planned to simulated the device's protection under extreme wave conditions were successfully executed in still water using a remotely operated ballast/de-ballast circuit. Results showed that further research is needed to overcome wave-induced instabilities for extreme wave conditions at low water depths.

Future research will apply the experimental results to validate numerical models and improve the UGEN's structural design and moorings configuration. These developments will reduce the uncertainty associated with the estimations of the cost of energy.

CRedit authorship contribution statement

S. Ribeiro e Silva: Conceptualization, Methodology, Investigation, Resources, Validation, Writing - original draft, Project administration. **R.P.F. Gomes:** Conceptualization, Methodology, Software, Validation, Formal analysis, Writing - original draft, Visualization. **B.S. Lopes:** Software, Formal analysis, Investigation, Visualization, Writing - original draft. **A.A.D. Carrelhas:** Software, Investigation, Resources, Writing - original draft. **L.M.C. Gato:** Conceptualization, Methodology, Validation, Formal analysis, Resources, Funding acquisition, Writing - original draft, Supervision. **J.C.C. Henriques:** Software, Formal analysis, Writing - original draft. **J.M. Gordo:** Methodology, Investigation, Writing - review & editing. **A.F.O. Falcão:** Writing - review & editing, Supervision.

Declaration of Competing Interest

The authors declare that they have no known competing financial interests or personal relationships that could have appeared to influence the work reported in this paper.

Acknowledgements

The access to the University of Plymouth's ocean basin was funded by the European Commission's Horizon 2020 research and innovation programme, under MARINET2 (Marine Renewables Infrastructure Network) initiative, grant agreement No. 731084. This work was funded by the Portuguese Foundation for the Science and Technology (FCT), through IDMEC, under LAETA, project UIDB/50022/2020. The model was built by ASM Industries. A great appreciation is due to the Portuguese Navy Diving Centre for all the logistic support and technical expertise graciously dispensed to the UGEN's team during instrumentation and preliminary assessment of the water tightness of the scaled model.

References

- [1] Gunn K, Stock-Williams C. Quantifying the global wave power resource. *Renewable Energy* 2012;44:296–304. <https://doi.org/10.1016/j.renene.2012.01.101>.
- [2] Falcão AFO. Wave energy utilization: A review of the technologies. *Renew Sustain Energy Rev* 2010;14(3):899–918. <https://doi.org/10.1016/j.rser.2009.11.003>.
- [3] Ribeiro e Silva S, Pessoa N, Pessoa J. Asymmetric floating tank for wave energy conversion, Portuguese Patent PT 105368, [In Portuguese] (2010).
- [4] Falcão AFO, Gato LMC. Air turbines, in: Sayigh AA (Ed.), *Comprehensive renewable energy*, Vol. 8, Ocean energy, Elsevier, 2012, pp. 111–149. <https://doi.org/10.1016/B978-0-08-087872-0.00805-2>.
- [5] Falcão AFO, Henriques JCC, Gato LMC. Self-rectifying air turbines for wave energy conversion: A comparative analysis. *Renew Sustain Energy Rev* 2018;91:1231–41. <https://doi.org/10.1016/j.rser.2018.04.019>.
- [6] Salter SH. Wave power. *Nature* 1974;249:720–4. <https://doi.org/10.1038/249720a0>.
- [7] Cordonnier J, Gorintin F, De Cagny A, Clément AH, Babarit A. SEAREV: Case study of the development of a wave energy converter. *Renewable Energy* 2015;80:40–52. <https://doi.org/10.1016/j.renene.2015.01.061>.
- [8] Pozzi N, Bracco G, Passione B, Sirigu SA, Mattiazio G. PeWEC: Experimental validation of wave to PTO numerical model. *Ocean Eng* 2018;167:114–29. <https://doi.org/10.1016/j.oceaneng.2018.08.028>.
- [9] Crowley S, Porter R, Taunton DJ, Wilson PA. Modelling of the WITT wave energy converter. *Renewable Energy* 2018;115:159–74. <https://doi.org/10.1016/j.renene.2017.08.004>.
- [10] Clemente D, Rosa-Santos P, Taveira-Pinto F, Martins P, Paulo-Moreira A. Proof-of-concept study on a wave energy converter based on the roll oscillations of multipurpose offshore floating platforms. *Energy Convers Manag* 2020;224:113363. <https://doi.org/10.1016/j.enconman.2020.113363>.
- [11] Gawad AFA, Ragab SA, Nayfeh AH, Mook DT. Roll stabilization by anti-roll passive tanks. *Ocean Eng* 2001;28:457–69. [https://doi.org/10.1016/S0029-8018\(00\)00015-9](https://doi.org/10.1016/S0029-8018(00)00015-9).
- [12] Moaleji R, Greig AR. On the development of ship anti-roll tanks. *Ocean Eng* 2007;34:103–21. <https://doi.org/10.1016/j.oceaneng.2005.12.013>.
- [13] Sheng W. Power performance of BBDB OWC wave energy converters. *Renewable Energy* 2019;132:709–22. <https://doi.org/10.1016/j.renene.2018.07.111>.
- [14] Portillo JCC, Reis PF, Henriques JCC, Gato LMC, Falcão AFO. Backward bent-duct buoy or forward bent-duct buoy? Review, assessment and optimisation. *Renew Sustain Energy Rev* 2019;112:353–68. <https://doi.org/10.1016/j.rser.2019.05.026>.
- [15] Falnes J. *Ocean waves and oscillating systems: linear interactions including wave-energy extraction*, Cambridge University Press, 2002. <https://doi.org/10.1017/CBO9780511754630>.
- [16] McCabe AP. Constrained optimization of the shape of a wave energy collector by genetic algorithm. *Renewable Energy* 2013;51:274–84. <https://doi.org/10.1016/j.renene.2012.09.054>.
- [17] Babarit A, Clément AH. Optimal latching control of a wave energy device in regular and irregular waves. *Appl Ocean Res* 2006;28:77–91. <https://doi.org/10.1016/j.apor.2006.05.002>.
- [18] Babarit A. A database of capture width ratio of wave energy converters. *Renewable Energy* 2015;80:610–28. <https://doi.org/10.1016/j.renene.2015.02.049>.
- [19] Fonseca N, Pessoa J, Ribeiro e Silva S, Le Boulluec M, Ohana J. Model tests of a wave energy converter based on water oscillating in a U tank, in: *Proceedings of the 12èmes Journées de l'Hydrodynamique*, Nantes, France, 2010.
- [20] Fonseca N, Pessoa J, Ribeiro e Silva S. Structuring the European Research Area, Research Infrastructure/Transnational Access, Contract No 026010 (METRI-UGEN), [Report] (2010).
- [21] Fonseca N, Ribeiro e Silva S, Pessoa J. Numerical modelling and assessment of the UGEN floating wave energy converter. *Int J Mar Eng* 2011;153:A115–A124, The Royal Inst. of Nav. Arch. <https://doi.org/10.3940/rina.ijme.2011.a2.wf6>.
- [22] Fonseca N, Pessoa J. Numerical modeling of a wave energy converter based on a U-shaped interior oscillating water column. *Appl Ocean Res* 2013;40:60–73. <https://doi.org/10.1016/j.apor.2013.01.002>.
- [23] Ribeiro e Silva S, Gomes RPF, Falcão AFO. Hydrodynamic optimization of the UGEN: Wave energy converter with U-shaped interior oscillating water column. *Int J Mar Energy* 2016;15:112–126. <https://doi.org/10.1016/j.ijome.2016.04.013>.
- [24] Curran R, Gato LMC. The energy conversion performance of several types of Wells turbine designs. *Proc Inst Mech Engrs* 1997;211(2):133–45. <https://doi.org/10.1243/0957650971537051>.
- [25] Falcão AFO, Gato LMC, Nunes EPAS. A novel radial self-rectifying air turbine for use in wave energy converters. *Renewable Energy* 2013;50:289–98. <https://doi.org/10.1016/j.renene.2012.06.050>.
- [26] Carrelhas AAD, Gato LMC, Henriques JCC, Falcão AFO, Varandas J. Test results of a 30 kW self-rectifying biradial air turbine-generator prototype. *Renew Sustain Energy Rev* 2019;109:187–98. <https://doi.org/10.1016/j.rser.2019.04.008>.
- [27] H2020 OPERA project, OPERA - open sea operating experience to reduce wave energy cost, H2020 project, European Commission, url: <http://opera-h2020.eu/> (2016–2019).
- [28] Ribeiro e Silva S, Santos TA, Guedes Soares C. Parametrically excited roll in regular and irregular head seas. *Int Shipbuild Progr* 2005;52(1):29–56.
- [29] Ribeiro e Silva S, Guedes Soares C. Prediction of parametric rolling in waves with a time domain non-linear strip theory model. *Ocean Eng* 2013;72:453–69. <https://doi.org/10.1016/j.oceaneng.2013.07.011>.
- [30] Gomes RPF, Malvar Ferreira JDC, Ribeiro e Silva S, Henriques JCC, Gato LMC. An experimental study on the reduction of the dynamic instability in the oscillating water column spar buoy, in: *Proc. of the 12th European Wave and Tidal Energy Conference*, Cork, Ireland, 2017.
- [31] Falcão AFO, Henriques JCC. Oscillating-water-column wave energy converters and air turbines: A review. *Renewable Energy* 2015;85:1391–424. <https://doi.org/10.1016/j.renene.2015.07.086>.
- [32] Coleman HW, Steele WG. Engineering application of experimental uncertainty analysis. *AIAA J* 1995;33(10):1888–96. <https://doi.org/10.2514/3.12742>.

- [33] Gomes RPF, Henriques JCC, Gato LMC, Falcão AFO. Wave power extraction of a heaving floating oscillating water column in a wave channel. *Renewable Energy* 2016;99:1262–75. <https://doi.org/10.1016/j.renene.2016.08.012>.
- [34] Woodward MD, van Rijsbergen M, Hutchinson KW, Scott A. Uncertainty analysis procedure for the ship inclining experiment. *Ocean Eng* 2016;114:79–86. <https://doi.org/10.1016/j.oceaneng.2016.01.017>.
- [35] Faltinsen OM. *Sea Loads on Ships and Offshore Structures*. Cambridge University Press; 1990.
- [36] Gomes RPF, Henriques JCC, Gato LMC, Falcão AFO. Time-domain simulation of a slack-moored floating oscillating water column and validation with physical model tests. *Renewable Energy* 2020;149:165–80. <https://doi.org/10.1016/j.renene.2019.11.159>.
- [37] Giorgi G, Gomes RPF, Henriques JCC, Gato LMC, Bracco G, Mattiazzo G. Detecting parametric resonance in a floating oscillating water column device for wave energy conversion: Numerical simulations and validation with physical model tests. *Appl Energy* 2020;276:115421. <https://doi.org/10.1016/j.apenergy.2020.115421>.
- [38] Giorgi G, Gomes RPF, Bracco G, Mattiazzo G. Numerical investigation of parametric resonance due to hydrodynamic coupling in a realistic wave energy converter. *Nonlinear Dyn* 2020;101:153–70. <https://doi.org/10.1007/s11071-020-05739-8>.
- [39] Goda Y. *Random Seas and Design of Maritime Structures*. 3rd Edition., Singapore: World Scientific; 2010. doi:10.1142/7425.
- [40] Dean RG, Dalrymple RA. *Water Wave Mechanics for Engineers and Scientists*, World Scientific, 1991. <https://doi.org/10.1142/1232>.